





# An immunoregulation PLGA/Chitosan aligned nanofibers with polydopamine coupling basic fibroblast growth factor and ROS scavenging for peripheral nerve regeneration

Xiaokun Chen<sup>a,1</sup>, Jihai Xu<sup>b,1</sup>, Feng Qin<sup>c,d,e,1</sup> , Ziyuan Yang<sup>c,d,f</sup> ,  
Xueyuan Li<sup>g</sup>, Miao Yu<sup>g</sup>, Ming Li<sup>c,d,f,\*</sup>, Yanhua Wang<sup>c,d,e,\*\*</sup>,  
Wang Xin<sup>h,\*\*\*</sup>

<sup>a</sup> Ninth People's Hospital Affiliated to Shanghai Jiao Tong University School of Medicine, China

<sup>b</sup> Department of Hand Surgery, Department of Plastic Reconstructive Surgery, Ningbo No.6 Hospital, Ningbo, 315040, China

<sup>c</sup> Key Laboratory of Trauma and Neural Regeneration, Ministry of Education, Peking University, Beijing, 100044, China

<sup>d</sup> National Center for Trauma Medicine, Beijing, 100044, China

<sup>e</sup> Department of Orthopedics and Trauma, Peking University People's Hospital, Beijing, 100044, China

<sup>f</sup> Trauma Medicine Center, Peking University People's Hospital, Beijing, 100044, China

<sup>g</sup> Department of Hand Surgery, Ningbo No.6 Hospital, Ningbo, 315040, China

<sup>h</sup> Department of Plastic Reconstructive Surgery, Ningbo No.6 Hospital, Ningbo, 315040, China

## ARTICLE INFO

### Keywords:

Composite nerve conduits  
Electrospun nanofibers  
Polydopamine  
Immune modulation  
Peripheral nerve regeneration

## ABSTRACT

The repair and functional recovery of long-segment peripheral nerve injuries are crucial in clinical settings. Nerve conduits are seen as promising alternatives to autologous nerve grafts, but their effectiveness is limited by the controlled delivery of bioactive factors and meeting various functional requirements during different stages of repair. This research developed multifunctional nerve conduits using electrospinning and polydopamine (PDA) coating techniques to integrate bioactive substances. Chitosan-composite PLGA electrospun nerve conduits demonstrated exceptional mechanical properties and biocompatibility. Nanofibers with specific topological structures effectively promoted oriented cell growth. The PDA coating provided ROS scavenging and immune modulation functions. The bFGF growth factor attached to the PDA coating facilitated sustained release, enhancing Schwann cell functionality and stimulating neurite outgrowth. In a rat sciatic nerve defect model with a 10 mm gap, PLGA/CS-PDA-bFGF nerve conduits showed a positive impact on nerve regeneration and functional recovery. Consequently, nerve conduits with multiple functions modified with PDA-coated bioactive molecules are poised to be excellent materials for mending peripheral nerve injuries.

## 1. Introduction

Injuries to peripheral nerves are prevalent and can result in muscle paralysis, disability, neuropathic pain, and various other complications, thereby exerting a substantial influence on the quality of life of affected individuals [1–4]. In situations involving significant peripheral nerve damage resulting in gaps, the use of nerve grafts or nerve conduits is essential to promote the development of a regenerative pathway. Autologous nerve grafts remain the preferred method for addressing

nerve gaps and are widely regarded as the most effective approach in nerve repair [5–7]. Nevertheless, autologous nerve transplantation presents various challenges in the clinical setting. These challenges encompass the necessity for two surgical procedures at both the donor and recipient sites, the restricted supply of appropriate autologous nerves for transplantation, structural differences between the donor and recipient sites that may lead to mismatches, and the potential risk of neurogenic tumor development at the donor site [8,9]. The advancement of tissue engineering technology has led to the emergence of

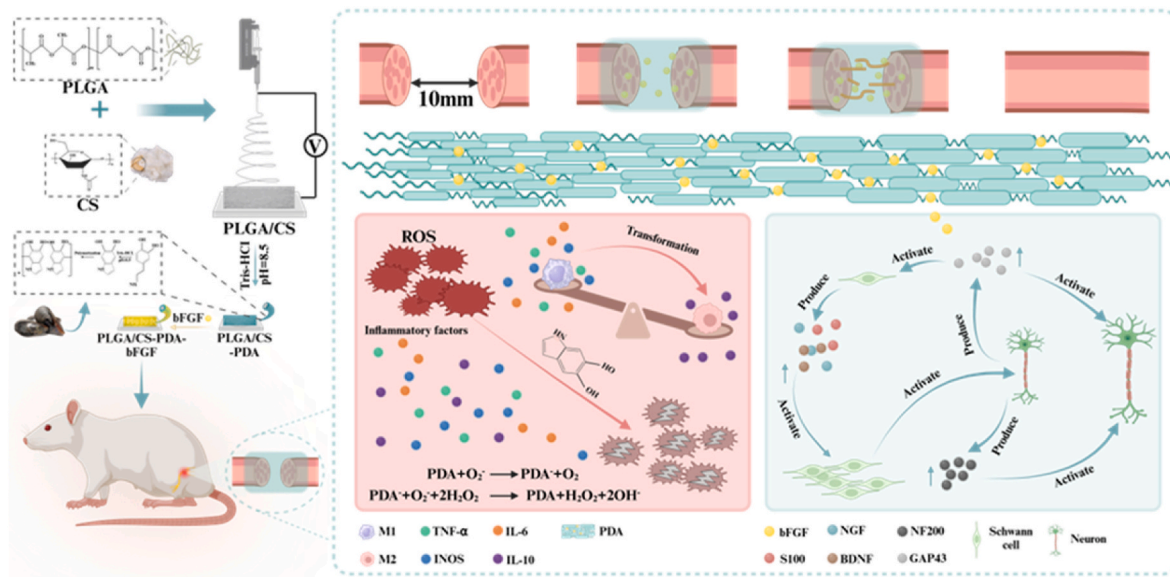
\* Corresponding author. Key Laboratory of Trauma and Neural Regeneration, Ministry of Education, Peking University, Beijing, 100044, China.

\*\* Corresponding author. Key Laboratory of Trauma and Neural Regeneration, Ministry of Education, Peking University, Beijing, 100044, China.

\*\*\* Corresponding author.

E-mail addresses: [liming\\_ort@bjmu.edu.cn](mailto:liming_ort@bjmu.edu.cn) (M. Li), [94719599@qq.com](mailto:94719599@qq.com) (Y. Wang), [dr.wangxin@qq.com](mailto:dr.wangxin@qq.com) (W. Xin).

<sup>1</sup> These authors contributed equally to this work.



**Scheme 1.** A nerve conduit scaffold was developed through the combination of natural chitosan and synthetic PLGA materials using electrospinning techniques. Through the application of PDA coating technology to incorporate the bioactive factor bFGF, the scaffold enabled in vivo delivery. This nerve conduit demonstrates the ability to address reactive oxygen species in the initial phases of nerve injury, promote M2 polarization of macrophages to modulate the regenerative microenvironment, improve Schwann cell functionality in subsequent repair stages, and direct axon elongation to facilitate peripheral nerve regeneration.

artificial nerve conduits as a viable alternative to autologous nerve grafts in the treatment of peripheral nerve injuries. This innovative approach has garnered significant interest and is considered a promising technology in the field [10].

Electrospinning apparatus utilized in material production are uncomplicated and economical, enabling the creation of nano-scale continuous fibers characterized by a substantial specific surface area and elevated porosity. These attributes are advantageous for emulating the natural extracellular matrix, rendering them well-suited materials for fabricating nerve conduits [11,12]. Moreover, thorough investigation suggests that early administration of antioxidants, development of myelin sheath, and stimulation of axonal growth are crucial focal points for enhancing the recovery of peripheral nerve damages [8,13–18]. Hence, it is imperative to develop electrospun channels that control the microenvironment, enhance the proliferation and movement of Schwann cells, and direct the growth of axons from the proximal to distal regions.

The electrospinning technique enables precise manipulation of fiber morphology, facilitating the alignment of nanofibers along the longitudinal axis or perpendicular orientations in both axial and radial planes [19,20]. Fibers engineered with a specific alignment can greatly improve the mechanical characteristics of scaffolds in the direction of the fiber axis, while also supporting cell growth, specialization, and aiding in nerve regeneration [21,22]. Furthermore, it is essential for nerve conduits to exhibit high biodegradability, mechanical strength similar to that of native tissues, and superior biocompatibility [23]. Hence, the selection of materials in the process of electrospinning plays a critical role in attaining desired properties. Chitosan, being a naturally occurring polymer with renewable characteristics, has garnered significant interest for its antimicrobial attributes, ability to inhibit tumor growth, facilitation of tissue regeneration and repair, and hemostatic properties [24,25]. Studies have shown that chitosan conduits have the ability to suppress the proliferation of fibroblasts, decrease fibrous scarring, and enhance the growth of endothelial cells, thus aiding in the process of nerve regeneration [26]. Chitosan's inherent mechanical limitations hinder its ability to meet the necessary compressive strength standards in clinical applications, thus impeding its effectiveness in repair processes. In contrast, PLGA (poly(lactic-co-glycolic acid)) offers the advantage of adjusting polymer strength and degradation rate

through the manipulation of the PLA (polylactic acid) to PGA (polyglycolic acid) ratio. The superior mechanical properties of PLGA can offset chitosan's brittleness. Consequently, the integration of natural and synthetic materials through electrospinning to create composite conduits with oriented structure, degradability, and enhanced mechanical characteristics presents a promising approach.

Following nerve damage, Schwann cells undergo a process of proliferation and migration, while axons elongate through growth cones with the objective of reestablishing nerve connectivity and ultimately restoring nerve functionality [27]. Schwann cells are essential in facilitating nerve regeneration through contact-mediated mechanisms, as they create Büngner bands that are abundant in nerve growth factors at the site of injury. These specialized structures support the regrowth of axons and provide guidance for the inward growth of regenerating axons [15,16]. The growth cones elongate through budding along Büngner bands into the distal nerves or organs, a process that is controlled by neurotrophic factors [16]. Studies have shown that the fundamental Fibroblast Growth Factor (bFGF) exhibits protective properties on damaged neurons, stimulates the growth of neuroglial cells, and aids in the regeneration of nerve fibers [28,29]. Nevertheless, the direct incorporation of growth factors during the spinning process may result in challenges such as growth factor deactivation caused by organic toxic solvents and unregulated release. A potential effective strategy could involve gently modifying the electrospun fibers post-production to enable drug loading and achieve sustained controlled release over an extended period. At present, techniques like sustained-release microspheres and hydrogel injections are employed to augment the bioactive properties of nerve conduits. Nevertheless, these methods introduce heightened intricacy and expenses to the manufacturing process. Hence, the imperative lies in the advancement of swift, uncomplicated, and economical approaches for the modification of bioactive factors.

Polydopamine (PDA) has garnered significant interest and investigation within the scientific community owing to its robust adhesion properties, elevated chemical reactivity, superior hydrophilicity, and favorable biocompatibility, among other notable attributes [30]. In alkaline conditions, dopamine undergoes oxidation and self-polymerization to generate nano-sized polydopamine films, which effectively maintain the microstructure of the underlying substrate surface. The surface of the PDA contains a high concentration of quinone

and amine functional groups, enabling potential covalent interactions with proteins or peptides via Michael addition or Schiff reaction mechanisms [31,32]. For instance, Zhu and colleagues demonstrated that bone scaffolds modified with polydopamine effectively encapsulate and continuously release VEGF, leading to the enhancement of vascular regeneration and functionalization [33]. Moreover, Repair of peripheral nerve injury relies on the reconstruction of the regenerative microenvironment. Four factors have been put forward to influence the microenvironment of nerve repair in peripheral nerve injury, namely angiogenesis, immune response, bioenergetic metabolism, and bioelectric conduction. Vascular endothelial cells, macrophages, fibroblasts, and Schwann cells collectively form the regenerative microenvironment of peripheral nerve injury [34]. Most of the current applications of medical materials in the repair of peripheral nerve injury revolve around rebuilding the regenerative microenvironment. Yuan Wei-En's team enhanced the PNI regenerative microenvironment by inducing immunometabolic reprogramming of macrophages using RGO@UIO-66/PCL scaffolds [35–37]. The initial inflammatory response following peripheral nerve injury leads to oxidative stress, resulting in an increased release of pro-inflammatory factors and exacerbating the inflammatory response. Excessive inflammation and oxidative stress disrupt the regenerative microenvironment and aggravate nerve tissue damage, leading to delayed or impaired nerve regeneration [38]. PDA can participate in the reconstruction of the regenerative microenvironment by scavenging ROS to promote the repair of peripheral nerve injuries. Hu et al. have documented the efficacy of PDA in ROS clearance, leading to the suppression of arthritis advancement [39]. Likewise, Bao et al. have highlighted PDA's ROS scavenging properties and its role in immune modulation for enteritis treatment [32]. To date, there is a lack of literature on the utilization of PDA for immune microenvironment regulation in peripheral nerve tissue engineering.

As shown in Scheme 1, we prepared oriented PLGA/CS-PDA-bFGF nerve conduits with multiple functions of early immunomodulation, scavenging of ROS, promotion of myelin sheath formation, and guidance of axon growth. Specifically, electrostatic spinning technology was used to construct oriented fiber nerve conduits of natural material chitosan and artificial material PLGA composites to provide growth and guidance space for nerve regeneration. Further coupling of bFGF after encapsulating PDA coating on the catheter surface, the PDA coating not only achieves efficient loading and slow release of bFGF for reinforcing the function of Schwann cells and promoting axon growth of neuronal cells, but also neutralizes excessive ROS as well as promotes macrophage phenotypic transformation in the early stage at the site of injury. In this study, based on the topographical guidance cues provided by the nerve conduit, PDA and bFGF were introduced to promote the repair of peripheral nerve injury through the modulation of Schwann cells, neuronal cells, and macrophages in order to construct a favorable regenerative microenvironment. We conducted experiments on the microscopic morphology observation, mechanical properties, degradation properties, drug loading and slow release, biocompatibility, in vitro antioxidant and immunomodulation of the catheters, and in vivo evaluation of the effect of sciatic nerve repair. We believe that a nerve conduit with multifunctional PDA-coated coupled bioactive molecules that regulate the regenerative microenvironment, strengthen the function of Schwann cells, and promote axon growth has great potential in peripheral nerve injury repair.

## 2. Materials and methods

### 2.1. Materials

PLGA was purchased from Jinan Daigang Bioengineering Co., Ltd. (Jinan, China). Chitosan (CS, degree of deacetylation: ~90 %) was obtained from Shanghai Aladdin Biochemical Technology Co., Ltd. (Shanghai, China). FITC-labeled neurotensin (FITC) was sourced from BIO-ZL (Beijing, China). 0.25 % trypsin, fetal bovine serum were

obtained from Gibco (Grand Island, New York, USA). PBS buffer was purchased from Logan (Logan, Utah, USA). FITC-labeled BSA, iNOS Polyclonal antibody, 5 % BSA blocking solution were obtained from Solarbio (Beijing, China). DAPI was sourced from SIGMA (Shanghai, China). Other reagents were purchased from China National Pharmaceutical Group Corporation and used directly.

### 2.2. Synthesis of scaffold

To begin the process, measure 18g of hexafluoroisopropanol and place it in a reaction vessel along with an appropriate magnetic stirring bar. Subsequently, measure 2g of PLGA powder and gradually introduce it into the hexafluoroisopropanol while maintaining continuous stirring. Close the vessel and stir the mixture at room temperature for a duration of 8 h until the PLGA powder is fully dissolved. The electrospinning conditions are configured as follows: a spinning voltage of +12.3 kV, a solution flow rate of 1.4 ml/h, and a collecting distance of 15 cm. The temperature and humidity levels are regulated at 28 °C and 45 %, respectively. Following the electrospinning process, retrieve the PLGA/CS scaffold and subject it to vacuum drying overnight at room temperature.

### 2.3. Coating of PDA layers

The PLGA/CS scaffold should be submerged in a dopamine solution (2 mg/ml in 10 mM Tris-HCl, pH 8.5, sourced from Sigma-Aldrich) at room temperature and agitated at a constant speed of 100 rpm for a duration of 12 h. Subsequently, the scaffold should be rinsed with deionized water, subjected to freeze-drying, and the resulting product collected as the PLGA/CS-PDA scaffold.

### 2.4. Characterization of the scaffold

The surface morphology of PLGA/CS and PLGA/CS-PDA scaffolds was examined through scanning electron microscopy (SEM) using a JSM-7900 F instrument from JEOL, Tokyo, Japan. Elemental composition analysis of the scaffold surfaces was conducted via energy-dispersive X-ray spectrometry (EDS) and elemental mapping. Fiber diameters of the scaffolds were determined by analyzing SEM images with Image-Pro Plus 6.0 software from Media Cybernetics, Rockville, MD, USA. The water contact angle of the scaffolds was measured using a water contact angle tester (OCA20, DataPhysics, Filderstadt). The mechanical properties, including elastic modulus and elongation at break, of the PLGA/CS and PLGA/CS-PDA scaffolds were evaluated using a universal testing machine (Model 5848, Instron, Norwood, MA, USA). The degradation rates of the scaffolds in phosphate-buffered saline (pH 7.4) at 37 °C over a three-month period were investigated. Weight loss was determined by calculating the difference between the initial weight and the remaining weight of the scaffolds, and degradation rates were calculated as the ratio of weight loss to the initial weight. To ensure the reproducibility of the tests, three samples were prepared for each scaffold group.

### 2.5. Loading and release of bFGF

The PLGA/CS and PLGA/CS-PDA scaffolds were sectioned into 12 × 12 mm squares and immersed in a 1 ml solution of bFGF (1 µg/ml in sterile double-distilled water) at ambient temperature for a duration of 12 h. Following the loading process with bFGF, the PLGA/CS-bFGF and PLGA/CS-PDA-bFGF scaffolds were rinsed with deionized water and subsequently subjected to freeze-drying. The residual quantity of bFGF in the supernatant was assessed in accordance with the guidelines provided by the manufacturer, utilizing the Human FGF basic ELISA Kit (Acme, Shanghai, China). The quantity of bFGF loaded was determined by calculating the disparity between the initial quantity of bFGF and the remaining amount in the supernatant. Subsequently, the drug loading

efficiency of BDNF was computed as the ratio of the loaded drug amount to the initial drug quantity.

To assess the spatial distribution of basic fibroblast growth factor (bFGF) on the scaffold, fluorescein isothiocyanate-labeled bovine serum albumin (FITC-BSA) was utilized as a surrogate for bFGF. Following loading with FITC-BSA, the scaffold underwent rinsing with deionized water. Visualization was conducted through confocal laser scanning microscopy (CLSM). For the investigation of bFGF release, PLGA/CS-bFGF and PLGA/CS-PDA-bFGF scaffolds measuring  $12 \times 12$  mm were placed in 2 ml of phosphate-buffered saline (PBS) and agitated at  $37^\circ\text{C}$  (100 rpm). Supernatant samples were collected at specified time points (3, 7, 14, and 28 days), with 1 ml withdrawn and replaced with fresh PBS each time. The release of bFGF from the scaffold was quantified using the Human FGF basic ELISA Kit. Subsequently, the bFGF release profile was generated by plotting the cumulative percentage release of bFGF against time.

## 2.6. Cell proliferation, migration, and morphological observation of RSC96 cells

Schwann cell proliferation on the fabricated scaffolds was evaluated through the utilization of the Cell Counting Kit-8 (CCK-8) assay. Schwann cells were seeded onto PLGA/CS, PLGA/CS-PDA, and PLGA/CS-PDA-bFGF scaffolds at a density of  $5 \times 10^4$  cells  $\text{cm}^{-2}$ . Following incubation for 1, 3, and 5 days, the specimens were rinsed with PBS and subsequently exposed to a 10 % CCK-8 solution. Absorbance readings were taken at a wavelength of 450 nm using a microplate reader (SpectraMax M2, Molecular Devices, Sunnyvale, CA, USA) after a 2-h incubation period. After 5 days of cultivation, the morphology of Schwann cells cultured on the scaffolds was examined using scanning electron microscopy (SEM) (JSM-7900F, JEOL) and confocal laser scanning microscopy (CLSM) (TCS-SP8, Leica). For SEM analysis, samples were washed with PBS, immersed in a 2.5 % glutaraldehyde solution (Sigma-Aldrich) at  $4^\circ\text{C}$  overnight, dehydrated with graded ethanol, critically dried using a critical point dryer, and coated with a layer of gold via sputter coating. Samples designated for CLSM observation were washed with PBS, fixed overnight at  $4^\circ\text{C}$  in 4 % paraformaldehyde (Solarbio), permeabilized with 0.5 % Triton X-100 (Solarbio), blocked with 5 % BSA (Solarbio), and then incubated overnight at  $4^\circ\text{C}$  with rabbit anti-S100 antibody (1:200, Sigma-Aldrich). Subsequent to washing procedures, the samples were stained with Alexa Fluor 594 anti-rabbit IgG (1:200, ZSGB-BIO, Beijing, China) for 2 h at room temperature, with cell nuclei counterstained using DAPI (Sigma-Aldrich).

RSC96 cells were cultured on PLGA/CS, PLGA/CS-PDA, and PLGA/CS-PDA-bFGF scaffolds at a seeding density of  $5 \times 10^5$  cells per well to establish a confluent monolayer. Following this, a sterile pipette tip was used to gently scratch the confluent cell layer. The migration of cells was monitored using a microscope at 24 and 48 h post-scratching, and the rates of migration were subsequently quantified.

## 2.7. Morphological observation of PC12 cells

PC12 cells were cultured on scaffolds made of PLGA/CS, PLGA/CS-PDA, and PLGA/CS-PDA-bFGF at a seeding density of  $4 \times 10^4$  cells per square centimeter. The cell/scaffold constructs were treated with Phalloidin-Alexa Fluor 594/488 (Abcam) to visualize cell morphology and organization. Subsequently, fluorescence intensity was quantitatively analyzed. Utilizing ImageJ software, a line was manually traced along the longest axis of each cell, and the angle of deviation from the average orientation of the scaffold arrangement was determined.

## 2.8. Intracellular antioxidant assay

RSC96, RAW264.7, and PC12 cells were cultured in 96-well plates at a density of  $8 \times 10^3$  cells per well. After 48 h, the culture medium was replaced with fresh medium, and hydrogen peroxide ( $\text{H}_2\text{O}_2$ ) solutions

were introduced to interact with the scaffolds in each cell group. Following a 5-h incubation at  $37^\circ\text{C}$  in the absence of light, cell viability was assessed using the CCK-8 assay. The antioxidant properties of the materials on cells were examined using an ROS assay kit. Subsequently, RSC96, RAW264.7, and PC12 cells were seeded at a concentration of  $3 \times 10^4$  cells/ml in 24-well plates containing the scaffolds and incubated for 72 h. Post-incubation, cells were rinsed twice with phenol red-free DMEM. Then, 400  $\mu\text{L}$  of 50  $\mu\text{M}$   $\text{H}_2\text{O}_2$  was added to each well and incubated for 2 h. After washing to remove  $\text{H}_2\text{O}_2$ , cells were treated with a 10 mM dichloro-dihydro-fluorescein diacetate (DCFH-DA) probe and incubated in the dark for 20 min. Subsequent washes were performed to eliminate any unreacted probe. Fluorescence microscopy was utilized to observe cellular ROS levels, and cell viability was assessed using the CCK-8 assay. The measured ROS levels were recorded, and the relative ROS levels in each sample were calculated by dividing the ROS detection values by the corresponding CCK-8 detection values.

The DPPH assay was employed to evaluate the capacity for scavenging free radicals. Initially, a solution of DPPH was prepared in ethanol with a concentration of 0.1 mM. Subsequently, the specimens were immersed in the solution and incubated at  $37^\circ\text{C}$  in the absence of light for 30 min. Following incubation, the absorbance levels of the specimens were determined at 519 nm utilizing an Agilent Cary5000 UV-VIS-NIR spectrophotometer (USA). The percentage clearance rate was computed using the formula: clearance rate (%) =  $(1 - A_m/A_s) \times 100$  %. In this equation,  $A_s$  denotes the initial absorbance of DPPH, while  $A_m$  signifies the absorbance of DPPH subsequent to its interaction with the specimen for 30 min.

## 2.9. Morphological observation of RAW264.7 cells

RAW cells were cultured in confocal dishes at a density of  $3 \times 10^4$  cells per well and treated with PLGA/CS, PLGA/CS-PDA, and PLGA/CS-PDA-bFGF scaffolds after 12 h. After an additional 24 h, the cells were fixed with 4 % paraformaldehyde, washed with PBS, permeabilized with Triton X-100, and blocked with bovine serum albumin. The cells were then stained with TRITC-Phalloidin and DAPI to visualize the actin arrangement in the cytoskeleton, which was observed and imaged using laser confocal microscopy.

## 2.10. Real-time quantitative polymerase chain reaction

Following a 3-day incubation period, total RNA was isolated from RSC96, PC12, and RAW264.7 cell cultures cultivated on these substrates utilizing an RNA purification kit (ES Science, Shanghai, China). The isolated RNA was subsequently transcribed in the reverse direction into complementary DNA (cDNA) employing a reverse transcription kit (ABM, Vancouver, Canada). Following this, quantitative real-time polymerase chain reaction (qRT-PCR) was conducted on a CFX96TM real-time PCR system (Bio-Rad, Hercules, CA, USA) utilizing SYBR Green Realtime PCR Master Mix (TOYOBO, Osaka, Japan) for quantification. The expression levels of pertinent genes were determined utilizing the  $2^{-\Delta\Delta\text{Ct}}$  method and standardized against the reference gene GAPDH. The primer sequences for S100, NGF, BDNF, NF200, GAP43, Tubb3, TNF- $\alpha$ , iNOS, IL-6, and IL-10 are available in [Supplementary Table S1](#).

## 2.11. In vivo biosafety evaluation

The animal experiments conducted in this study were authorized by the Animal Ethics Committee of Peking University People's Hospital under Approval No. 2023PHE062. Tissue compatibility was assessed by implanting samples into the dorsal skin of female Sprague-Dawley rats weighing around 200g. The rats were initially anesthetized using pentobarbital sodium, following which specimens measuring  $10 \times 5$  mm were implanted into the subcutaneous tissue on their dorsal region ( $n = 3/\text{group}/\text{time point}$ ). Euthanasia of the rats was carried out on days 3, 7, and 14. The excised tissues were then fixed in 4 % paraformaldehyde for



24 h, dehydrated in a 30 % sucrose solution for 48 h, and stored at  $-80^{\circ}\text{C}$ . Subsequently, tissue sections were prepared and stained with hematoxylin and eosin (H&E) to evaluate the adjacent tissues. Immunofluorescent staining for Tumor Necrosis Factor-alpha (TNF- $\alpha$ ) and Interleukin-6 (IL-6) was conducted to assess the inflammatory response.

## 2.12. Animal experiments

The animal experiments were approved by the Animal Ethics Committee of Peking University People's Hospital (Approval No. 2023PHE062) and in accordance with the National Research Council's Guide for Care and Use of Laboratory Animals. Forty healthy female SD rats, each weighing around 200g, were procured from Beijing Vital River Laboratory Animal Technology Co., Ltd. All SD rats were housed in pathogen-free animal rooms, with the room maintained on a 12-h light/12-h dark cycle at  $20^{\circ}\text{C}$ . All SD rats were given free access to standard

chow and water ad libitum.

These rats were randomly divided into four groups: autograft group, PLGA/CS group, PLGA/CS-PDA group, and PLGA/CS-PDA-bFGF group, with 10 rats in each group. Nerve conduits, measuring 12 mm in length and 2 mm in inner diameter, were created by rolling the PLGA/CS, PLGA/CS-PDA, and PLGA/CS-PDA-bFGF scaffolds. Anesthesia was induced in all rats using 3 % isoflurane inhalation. Following shaving and disinfection, a 10 mm nerve segment was excised at the mid-femoral level of the right sciatic nerve. In the autograft group, the nerve segment was longitudinally flipped  $180^{\circ}$  and sutured back to the nerve stump using 8/0 nylon sutures. In the remaining groups, the proximal and distal nerve stumps were sutured into the nerve conduits at a depth of 1 mm using 8/0 nylon sutures. The muscle and skin incisions were subsequently closed with 4/0 nylon sutures.

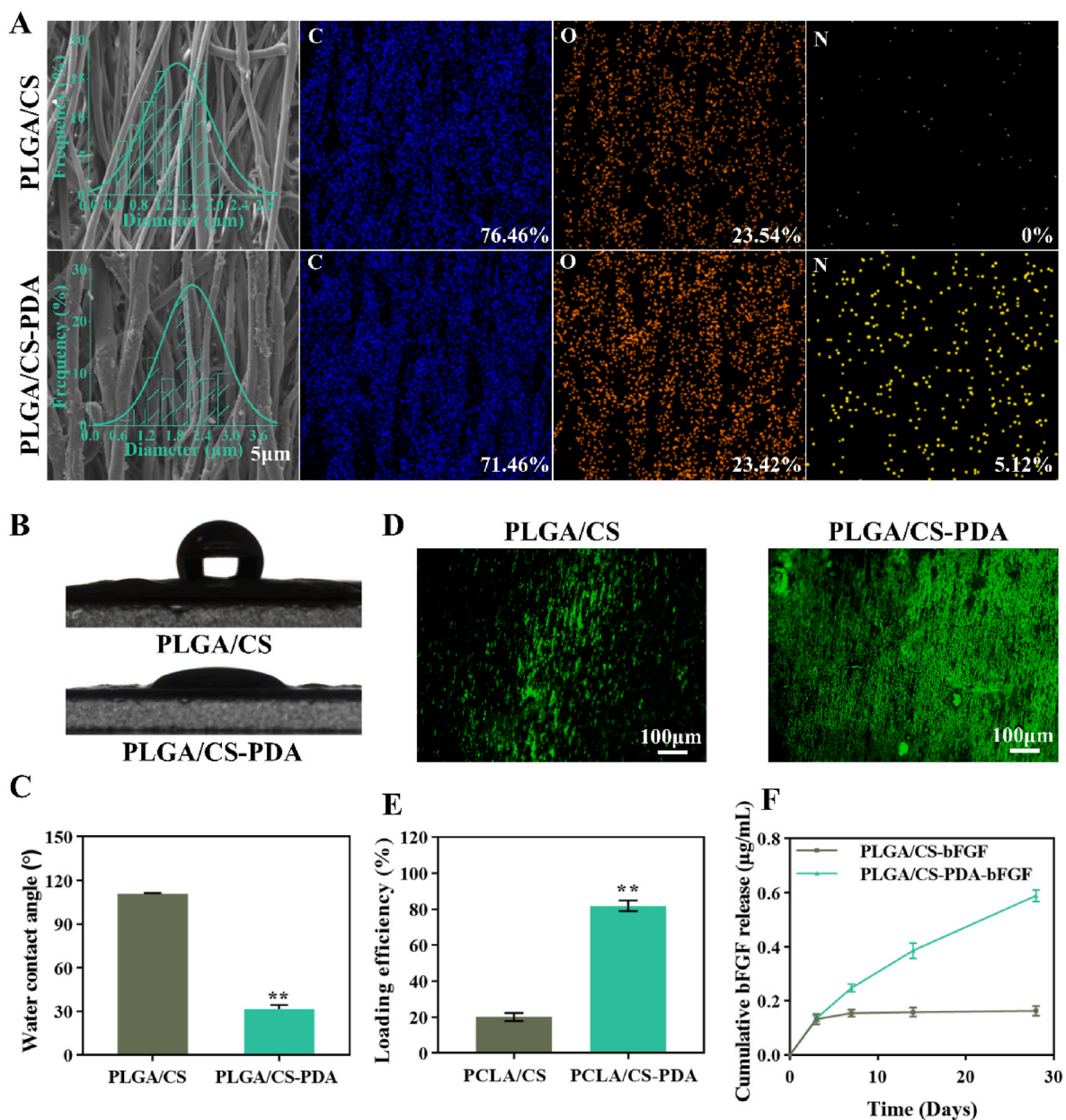


**Fig. 1.** (A) SEM and EDS elemental mapping images and fiber diameter distribution of PLGA/CS and PLGA/CS-PDA scaffolds. (B,C) Water contact angles of PLGA/CS and PLGA/CS-PDA scaffolds ( $n = 3$ ,  $**P < 0.01$ ). (D) CLSM images of FITC-BSA loaded onto PLGA/CS and PLGA/CS-PDA scaffolds. (E) Loading efficiency of bFGF from PLGA/CS and PLGA/CS-PDA scaffolds ( $n = 3$ ,  $**P < 0.01$ ). (F) Cumulative release of bFGF from PLGA/CS-bFGF and PLGA/CS-PDA-bFGF scaffolds.

### 2.13. SFI index

At the 12-week postoperative mark, the gait analysis system from Noldus in Wageningen, Netherlands was utilized to record the footprints of rats. The system measured various parameters such as Experimental Toe Spread (ETS), Normal Toe Spread (NTS), Experimental Print Length (EPL), Normal Print Length (NPL), Experimental Inter-Toe Spread (EIT), and Normal Inter-Toe Spread (NIT). Following this, the sciatic nerve function index (SFI) was determined by applying the formula:  $SFI = 109.5(ETS - NTS)/NTS - 38.3(EPL - NPL)/NPL + 13.3(EIT - NIT)/NIT - 8.8$ .

### 2.14. Electrophysiological testing

At the 12-week postoperative mark, a total of six rats from each experimental group were anesthetized for the purpose of conducting electrophysiological assessments on the previously injured sciatic nerve. During this procedure, two stimulating electrodes were strategically positioned 5 mm apart at both the proximal and distal ends of the regenerated nerve, while recording electrodes were inserted into the gastrocnemius muscle. Subsequent to this setup, compound muscle action potentials (CMAPs) of the gastrocnemius muscle were measured utilizing a neurophysiological system (Keypoint, Nørresundby, Denmark) with a current intensity of 3.0 mA at a frequency of 1 Hz. The CMAP amplitudes and latencies were then recorded and compared across the different groups to evaluate the recovery of nerve function.

### 2.15. Histological evaluation of gastrocnemius muscle

At 12 weeks post-surgery, the superficial blood was extracted from the gastrocnemius muscle at the transplant site, and the weight of the muscle was documented. The control group is referred to as Mc, while the group that underwent surgery is denoted as Ms. The formula for calculating the wet weight ratio of the gastrocnemius muscle is expressed as:  $T = (Mc - Ms)/Mc \times 100\%$ . Subsequently, the gastrocnemius muscles were embedded in paraffin, sliced into 5- $\mu$ m-thick sections, and stained with Masson's trichrome stain. Ten muscle sections were randomly chosen from each group, imaged using a Leica DM4B microscope. Six sections were then randomly selected, and the cross-sectional area of muscle fibers was measured using Image Pro Plus 6.0 software (Media Controllers), followed by statistical analysis.

### 2.16. Regenerative neurohistological assessment

Two weeks post-modeling, the central portions of regenerated nerves were encased in optimal cutting temperature compound (Sakura Finetek, Torrance, CA, USA) and cut into 12- $\mu$ m-thick slices. Subsequently, ten randomly chosen nerve slices from each cohort were subjected to immunofluorescence double-labeling. The samples were exposed to primary antibodies (at a 1:200 dilution for CD86, CD206, IL-6, TNF- $\alpha$ ) and secondary antibodies (Alexa Fluor 594 and 488, at a 1:1000 dilution), followed by DAPI staining. Visualization and quantitative assessment were conducted using confocal microscopy.

Twelve weeks post-modeling, the central portions of regenerated nerves were encased in optimal cutting temperature compound (Sakura Finetek, Torrance, CA, USA) and sectioned into 12- $\mu$ m-thick slices. Subsequently, ten randomly chosen nerve slices from each cohort underwent dual-label immunofluorescence. Primary antibodies utilized were rabbit anti-S100 (1:200, Sigma-Aldrich) and mouse anti-NF200 (1:200, Sigma-Aldrich), followed by secondary antibodies Alexa Fluor 594 anti-rabbit IgG (1:200, ZSGB-BIO) and Alexa Fluor 488 anti-mouse IgG (1:200, ZSGB-BIO). DAPI staining (Sigma-Aldrich) was conducted, and images were captured using confocal laser scanning microscopy (CLSM, TCS-SP8, Leica). Five random fields of view per slice were selected for each specimen, and Image-Pro Plus 6.0 software (Media Cybernetics) was employed for statistical analysis to determine the

proportion of S100-positive staining area and NF200-positive staining area.

The regenerated nerve's distal segments were encased in resin, then cut into 700 nm semi-thin sections and 70 nm ultra-thin sections. From each group, ten semi-thin sections were chosen randomly for toluidine blue staining. Utilizing a Leica DM4B microscope, images were taken. Five fields of view were randomly selected for each section, and myelinated nerve fiber density was measured using Image-Pro Plus 6.0 software (Media Cybernetics). Additionally, ten randomly selected ultra-thin sections were stained with uranyl acetate-lead citrate and imaged with a JEM-1400 electron microscope (Leica). Ten sections were randomly selected to measure myelin sheath thickness and myelinated nerve fiber diameter using Image-Pro Plus 6.0 software (Media Cybernetics).

### 2.17. Statistical analysis

In the study, numerical data were presented as mean values accompanied by standard deviations. Group comparisons were performed using Student's t-test for two-group comparisons and one-way analysis of variance (ANOVA) followed by Tukey's post hoc test for multiple group comparisons. Statistical analyses were carried out utilizing SPSS 22.0 software (IBM SPSS, Chicago, IL, USA). Statistical significance was defined as  $P < 0.05$ .

## 3. Results and discussion

### 3.1. Characterization of the scaffold

The microstructure and surface chemical element distribution of the produced scaffolds were examined through scanning electron microscopy (SEM) and energy-dispersive X-ray spectroscopy (EDS), as depicted in Fig. 1A. Both scaffold fibers exhibited alignment, with the PLGA/CS scaffold having an average fiber diameter of  $1.41 \pm 0.52 \mu\text{m}$  and the PLGA/CS-PDA scaffold having a diameter of  $2.18 \pm 0.64 \mu\text{m}$ . Following PDA modification, a slight increase in fiber diameter and surface roughness was observed, indicating the successful PDA modification of the PLGA/CS scaffold. Elemental mapping images revealed an increase in nitrogen (N) content from 0 % to 5.12 % in the PLGA/CS-PDA scaffold compared to the PLGA/CS scaffold, providing further evidence of the effective PDA coating modification.

Effective cell adhesion is an essential requirement for the successful integration of tissue engineering scaffolds [40]. In a specific spectrum, increased hydrophilicity proves advantageous for promoting cell adhesion and proliferation [41]. The hydrophilicity of the scaffolds was assessed through water contact angle measurements. Fig. 1B illustrates that the water contact angle of the PLGA/CS scaffold was  $110.8 \pm 0.43^\circ$ , whereas that of the PLGA/CS-PDA scaffold was  $31.51 \pm 0.49^\circ$ . The modification with PDA notably increased the hydrophilicity of the scaffold.

It is essential to create nerve conduits that are in alignment with the neuroregeneration process and have the capability to continuously release neurotrophic factors for an extended duration. Basic Fibroblast Growth Factor (bFGF) is a vital mitogenic factor with multifunctional properties that exert substantial impacts on neuronal cells [42]. In this study, FITC-BSA was employed as a representative drug to mimic the loading process of bFGF. The results illustrated in Fig. 1D indicate that the fluorescence intensity observed in the PLGA/CS-PDA group was notably greater compared to that in the PLGA/CS group. Furthermore, as demonstrated in Fig. 1E, the bFGF loading efficiency within the PLGA/CS-PDA group was measured at  $81.83 \pm 2.91\%$ , a value significantly exceeding that of the PLGA/CS group ( $P < 0.01$ ). The graph in Fig. 1F illustrates the release pattern of basic fibroblast growth factor. When comparing the PLGA/CS group to the PLGA/CS-PDA group, the former bFGF was released in large quantities in the first three days, while in the latter, it exhibited sustained and gradual release over a

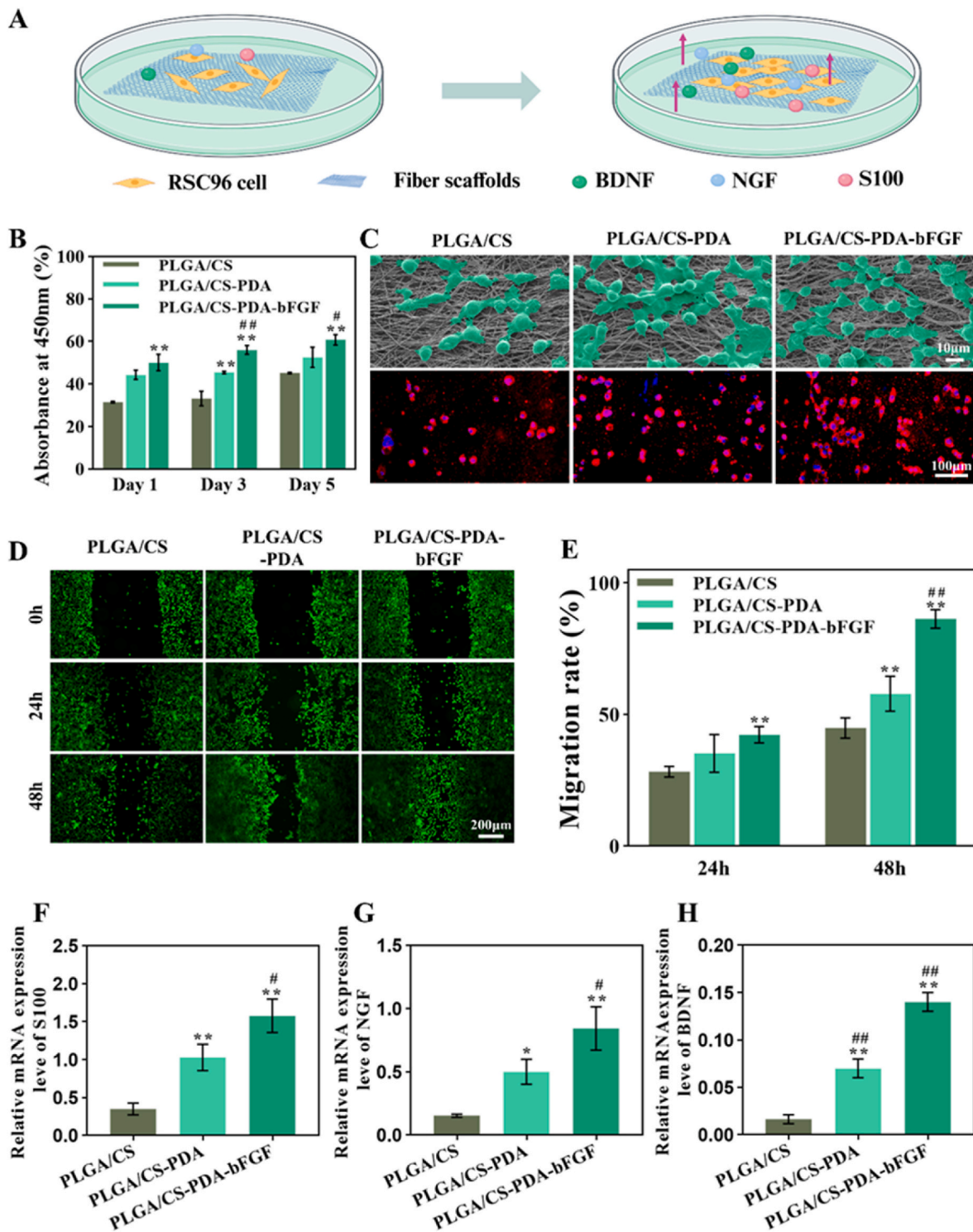


**Fig. 2.** (A) Schematic diagram of conducting experiments on RSC96 cells. (B) Proliferation of Schwann cells grown on PLGA/CS, PLGA/CS-PDA and PLGA/CS-PDA-bFGF scaffolds (n = 3, \*\* P < 0.01, versus PLGA/CS group). (C) SEM and CLSM images of Schwann cells grown on PLGA/CS, PLGA/CS-PDA and PLGA/CS-PDA-bFGF scaffolds. Fluorescent indicator used was Alexa Fluor 594 for S100 (red), and the nuclei were stained with DAPI (blue). (D,E) Migration images and migration rates of RSC96 cells on the different scaffolds. (F–H) Relative mRNA expression levels of S100, NGF and BDNF (n = 3, \*P < 0.05, versus PLGA/CS group; \*\*P < 0.01, versus PLGA/CS group; #P < 0.05, versus PLGA/CS-PDA group; ##P < 0.01, versus PLGA/CS-PDA group).

period of one month. In this study, the PLGA/CS - PDA - bFGF scaffold achieved local controlled release of bFGF through a PDA coating, with an average daily concentration of  $21.02 \pm 0.62$  ng/ml. Previous research on the promotion of peripheral nerve injury repair by bFGF has demonstrated that maintaining the local concentration of bFGF within the range of 4.29–67.25 ng/mL is conducive to improving the

regenerative microenvironment and promoting axon regeneration [43, 44]. These research results indicate that after adding bFGF to the PLGA/CS - PDA scaffold, bFGF can be released continuously over an extended period. This will be beneficial for the process of peripheral nerve regeneration. The mechanism of drug slow release of polydopamine coating can be explained from three aspects: diffusion,



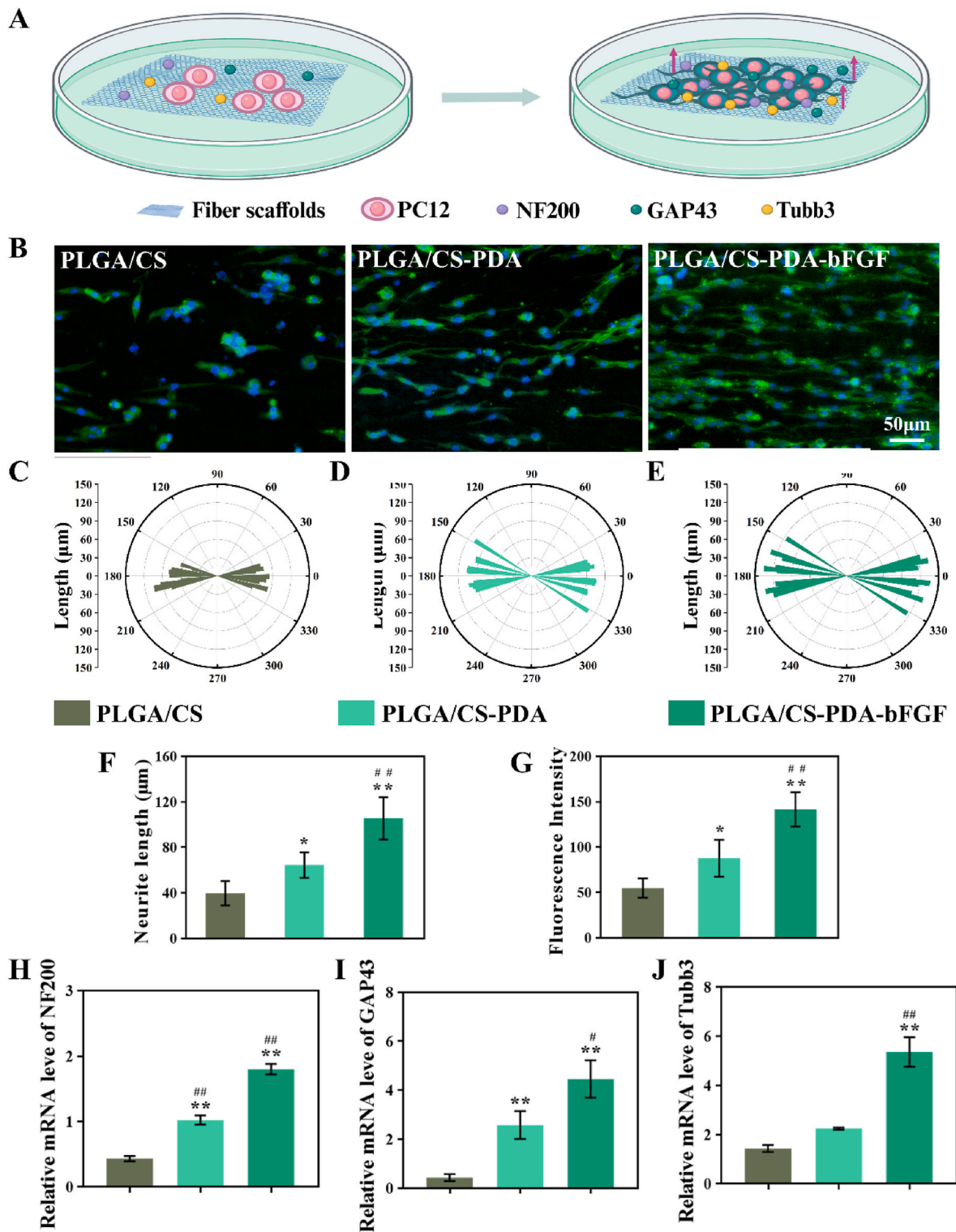


**Fig. 3.** (A) Schematic diagram of conducting experiments on PC12 cells. (B,C) Average neurite lengths of each group (\* $p < 0.05$  and \*\* $p < 0.01$ ). (D) Fluorescence Intensity of each group (\* $p < 0.05$  and \*\* $p < 0.01$ ). (E–G) Polar histograms of neurite orientation distribution showing the neurite growth of PC12 cell alignment along the direction of PLGA/CS, PLGA/CS-PDA and PLGA/CS-PDA-bFGF scaffolds. (H,I) Relative mRNA expression levels of NF200 and GAP43 ( $n = 3$ , \*\* $p < 0.01$ , versus PLGA/CS group; # $p < 0.05$ , versus PLGA/CS-PDA group; ## $p < 0.01$ , versus PLGA/CS-PDA group).

self-degradation, and disruption of surface adsorption-desorption equilibrium. Firstly, polydopamine has a certain pore structure, and the growth factor molecules move randomly in the pores, and due to the existence of a concentration gradient, they will diffuse from the inside of the polydopamine of high concentration to the outside of the low concentration environment. Secondly, the chemical structure of

polydopamine contains a variety of reactive groups, such as phenolic hydroxyl groups and amino groups, which may react chemically with substances in the surrounding environment, thus leading to the degradation of polydopamine. Degradation is relatively slow in an environment with a physiological pH value of about 7.4. In addition, the surface of polydopamine is rich in functional groups that can adsorb growth



factors. As the adsorption equilibrium is disturbed by changes in environmental conditions such as changes in solution composition, changes in temperature, etc., the growth factors are desorbed from the surface of polydopamine and thus released [45,46]. Over time, the polydopamine (PDA) coating in the body facilitates the gradual release of basic fibroblast growth factor (bFGF) through the progressive degradation of the PDA coating and the cleavage of covalent bonds. Furthermore, results from tensile testing reveal that the mechanical properties of the scaffold remain unaffected by PDA modification and bFGF loading, as depicted in Fig. S1. Fig. S2 displays the degradation rates of the three stent types after three months, all approximately at 6 % with no notable variances. This suggests that the stents can uphold their structural strength throughout the nerve regeneration phase, offering effective support and safeguarding for the regenerating nerves.

### 3.2. Effects of scaffold groups on schwann cell behavior

Schwann cells play a crucial role in the nerve repair process, with alterations in their activity and functionality impacting the success of nerve regeneration. In order to assess the impact of various scaffolds such as PLGA/CS, PLGA/CS-PDA, and PLGA/CS-PDA-bFGF on the biological behavior of Schwann cells, a series of biocompatibility, proliferation, and migration assays were performed on RSC96 cells, as depicted in Fig. 2A. The findings from the CCK-8 assay, illustrated in Fig. 2B, demonstrate a rise in cell numbers over time across all groups, implying low cytotoxicity of the scaffolds towards the cells. Specifically, the cell counts within the PLGA/CS-PDA and PLGA/CS-PDA-bFGF scaffold groups were notably greater compared to the PLGA/CS scaffold group ( $P < 0.01$ ). Additionally, the group utilizing the PLGA/CS-PDA-bFGF scaffold exhibited a higher cell count in comparison to the group using the PLGA/CS-PDA scaffold ( $P < 0.05$ ). The cellular morphology of RSC96 cells cultured on each scaffold for a duration of 3 days is illustrated in Fig. 2C. The scanning electron microscopy (SEM) images illustrate spindle-shaped cells proliferating along the scaffold fibers. Conversely, confocal laser scanning microscopy (CLSM) images demonstrate that the cell density is most pronounced on the PLGA/CS-PDA-bFGF scaffold, followed by the PLGA/CS-PDA scaffold, and least on the PLGA/CS scaffold. These findings suggest that the oriented structure of the PLGA/CS-PDA-bFGF scaffold influences the alignment of Schwann cell growth. The increased hydrophilicity resulting from PDA modification and the incorporation of the growth factor bFGF both facilitate the attachment and expansion of RSC96 cells. Scaffolds with PDA coating to promote the proliferation of Schwann cells involve three functions of dopamine. First, because PDA is rich in hydrophilic functional groups such as amino and carboxyl groups, the increased hydrophilicity of scaffolds surface-modified with PDA can promote the attachment and proliferation of Schwann cells. Secondly, the strong adhesive property of dopamine can increase the interaction between the cell and the scaffold. Thirdly, the protein loading rate of the scaffolds modified with PDA will be significantly increased, so after loading bFGF, the superimposed benefit of the two effects with the high adhesive property of polydopamine will promote the proliferation of Schwann cells more obviously.

The removal of myelin debris is essential for the repair of nerves, with the rapid and thorough clearance of such debris being of utmost importance. The timely migration of Schwann cells is a significant factor in facilitating the clearance of myelin debris. The figures illustrate the migration images and rates of Schwann cells, as indicated in Fig. 2D and E. Within the PLGA/CS-PDA-bFGF group, Schwann cells demonstrated the most notable migration rate, followed by the PLGA/CS-PDA group, with the PLGA/CS group displaying the least migration activity. Following the clearance of debris, Schwann cells undergo proliferation and organize into Büngner bands surrounding the site of injury. These bands serve as conduits for axonal growth, facilitating the inward regeneration of axons. Moreover, Schwann cells release a variety of substances that establish an optimal microenvironment to support the

regeneration of nerves [47]. In this study, the impact of scaffolds composed of PLGA/CS, PLGA/CS-PDA, and PLGA/CS-PDA-bFGF on the mRNA expression levels of S100, NG, and BDNF released by Schwann cells was further assessed through PCR analysis. The results depicted in Fig. 2F–H reveal a significant upregulation in the relative expression levels of S100, NGF, and BDNF within the PLGA/CS-PDA-bFGF group compared to both the PLGA/CS and PLGA/CS-PDA groups ( $p < 0.05$  or  $p < 0.01$ ). Moreover, the PLGA/CS-PDA group demonstrated elevated expression levels in comparison to the PLGA/CS group ( $p < 0.05$  or  $p < 0.01$ ). These findings suggest that the PLGA/CS-PDA-bFGF scaffold exhibits enhanced efficacy in promoting Schwann cell proliferation and adhesion, as well as in stimulating the secretion of neurotrophic factors.

### 3.3. Impact of scaffold groups on neuronal cell behavior

bFGF is essential for the development and functionality of nerve cells, as it facilitates growth, differentiation, axonal growth, and synaptic formation. Its presence promotes the restoration and rejuvenation of impaired nerves, ultimately enhancing neural function [48,49]. In order to analyze the influence of individual scaffold groups on neuronal cells, we examined parameters such as neuronal cell proliferation, axon development, and secretion of neurotrophic factors. The experimental details are depicted in Fig. 3A.

The alignment of PC12 cells on PLGA/CS, PLGA/CS-PDA, and PLGA/CS-PDA-bFGF scaffolds is illustrated in Fig. 3B, demonstrating directional alignment compared to the random growth observed in the control group culture dish. This alignment suggests that fibers oriented in a specific direction can influence the directional extension of neuronal axons. The average lengths of axonal growth on each scaffold are presented in Fig. 3C:  $39.79 \pm 9.68 \mu\text{m}$  for PLGA/CS,  $64.40 \pm 10.07 \mu\text{m}$  for PLGA/CS-PDA, and  $105.55 \pm 16.96 \mu\text{m}$  for PLGA/CS-PDA-bFGF. The results presented in Fig. 3D illustrate the fluorescence intensities of PC12 cells. The findings suggest that the fluorescence intensities observed on PLGA/CS-PDA and PLGA/CS-PDA-bFGF scaffolds are significantly elevated compared to those on the PLGA/CS scaffold ( $p < 0.05$ ), indicating that the modification with PDA enhances neuronal cell adhesion and proliferation. Moreover, on the PLGA/CS-PDA-bFGF scaffold, there is a longer axonal growth length and higher fluorescence intensity in comparison to the PLGA/CS-PDA scaffold. This suggests that, in contrast to the PLGA/CS-PDA scaffold, the PLGA/CS-PDA-bFGF scaffold more effectively facilitates the growth and extension of neuronal cells.

NF200 is a distinctive indicator for neuronal cells, GAP43 is recognized as a marker protein for axonal growth in neuronal development and repair following injury, and Tubb3 serves as a marker for the transformation of stem cells into neurons [50]. Hence, polymerase chain reaction (PCR) was employed to assess the comparative mRNA expression levels of NF200, GAP43, and Tubb3 in order to authenticate the functional impacts of various scaffolds on neuronal cells. The results depicted in Fig. 3H–I indicate that the mRNA expression levels of NF200, GAP43, and Tubb3 were most pronounced on the PLGA/CS-PDA-bFGF scaffold, followed by the PLGA/CS-PDA scaffold ( $p < 0.01$ ), and least on the PLGA/CS scaffold ( $p < 0.05$ ). This observation further substantiates the notion that the PLGA/CS-PDA-bFGF scaffold effectively enhances the proliferation and differentiation of neuronal cells.

### 3.4. In vitro oxidative stress protection and immunomodulatory effects of scaffold groups

Overexpression of both pro-inflammatory and anti-inflammatory molecules, along with the buildup of reactive oxygen species (ROS), are recognized as contributing factors to neuronal injury [51]. Hence, it is imperative for neuronal regeneration that there is prompt removal of reactive oxygen species and a proactive adjustment to the microenvironment for immune regulation. Consequently, we illustrated the anti-oxidative potential of the PLGA/CS-PDA-bFGF scaffold through a series

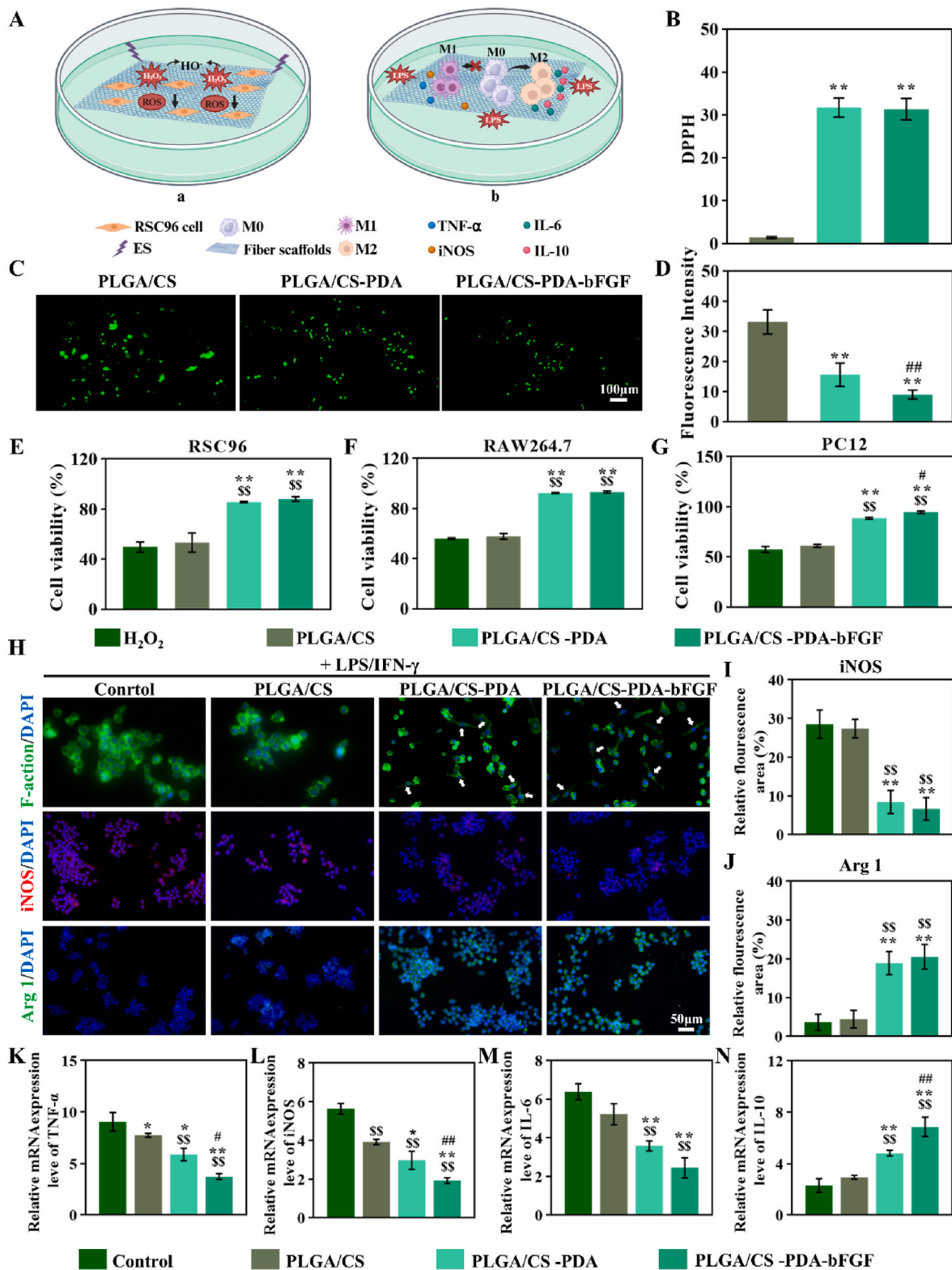


**Fig. 4.** (A) Schematic diagram of conducting experiments on RSC96 cells and RAW264.7 cells. (B) The DPPH method was used to evaluate the neutralizing ability of each group of scaffolds against free radicals. (C) Reactive oxygen staining (DCFH) of RSC96 cells cultured on the PLGA/CS, PLGA/CS-PDA, and PLGA/CS-PDA-bFGF with (+) or without (−) 50 μM H<sub>2</sub>O<sub>2</sub> stimulation. (D) The relative amount of ROS levels in RSC96 cells after H<sub>2</sub>O<sub>2</sub> stimulation was reacted by immunofluorescence intensity in each group. (E–G) Cellular activity of RSC96, PC12 and RAW264.7 cells in each group of scaffolds after H<sub>2</sub>O<sub>2</sub> treatment. (H) Microscopic fluorescence pictures showcasing the stained cytoskeleton and nucleus of RAW macrophages, either maintained in normal culture conditions or subjected to scaffolds co-culture for 24 h. Depiction of iNOS (red) and Arg-1 (green) differentiation clusters via fluorescence microscopy in RAW 264.7 macrophages after a 24-h period of inflammatory stimulation. (I, J) Statistics of the percentage of iNOS and Arg-1 immunofluorescence-positive zone. (K–N) Relative mRNA expression levels of TNF-α, iNOS, IL-6, and IL-10 (n = 3, \*P < 0.05, versus PLGA/CS group; \*\*P < 0.01, versus PLGA/CS group; #P < 0.05, versus PLGA/CS-PDA group; ##P < 0.01, versus PLGA/CS-PDA group; \$P < 0.05, versus PLGA/CS-PDA-bFGF group; \$\$P < 0.01, versus PLGA/CS-PDA-bFGF group).

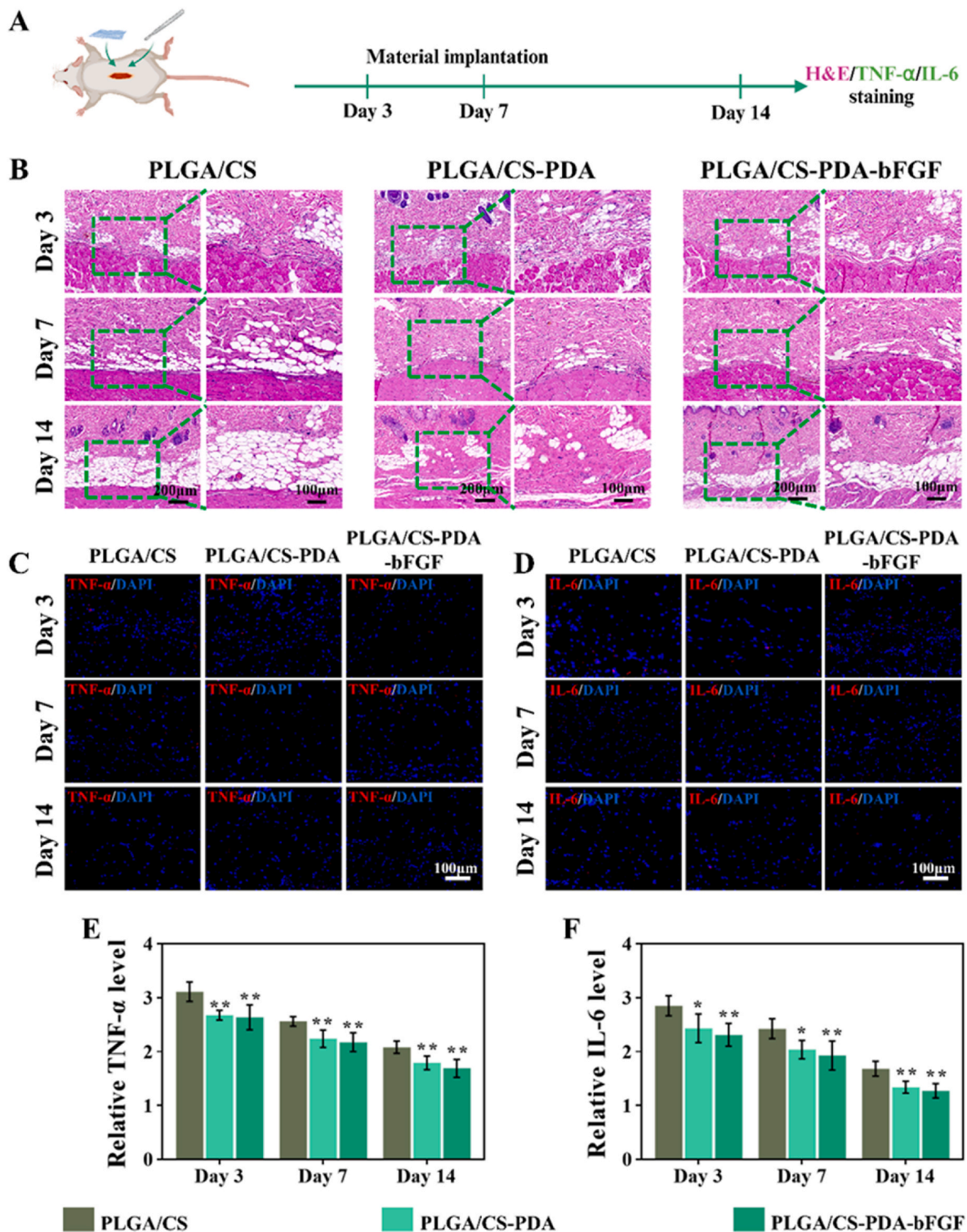
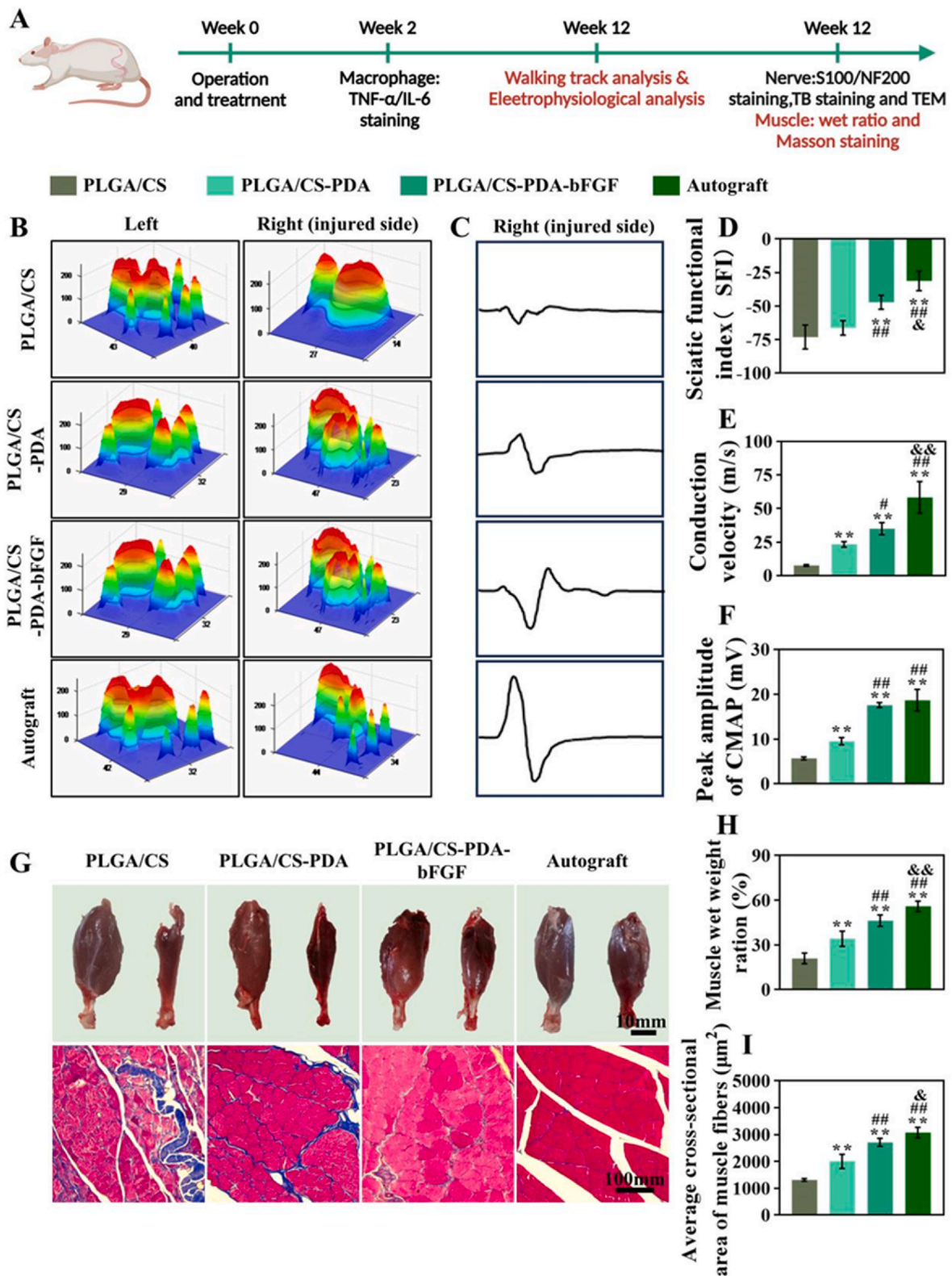


Fig. 5. (A) Histocompatibilities of the PLGA/CS, PLGA/CS-PDA, and PLGA/CS-PDA-bFGF scaffolds on 3, 7, and 14 days. (B) H&E staining. Scale bars: 200  $\mu$ m (left) and 100  $\mu$ m (right). (C) TNF- $\alpha$  immunofluorescence staining. Scale bar: 100  $\mu$ m. (E) Fluorescence statistical analysis (\* $p < 0.05$ ). (D) IL6 immunofluorescence staining. Scale bar: 100  $\mu$ m. (F) Fluorescence statistical analysis (\* $p < 0.05$  and \*\* $p < 0.01$ ).

of experiments (refer to Fig. 4A). Initially, we evaluated the capacity of the scaffolds to eliminate free radicals. The PLGA/CS-PDA and PLGA/CS-PDA-bFGF groups demonstrated enhanced scavenging efficacy in comparison to the PLGA/CS group (refer to Fig. 4B). Upon exposure to H<sub>2</sub>O<sub>2</sub>, the fluorescence intensity of the PLGA/CS group notably exceeded that of the PLGA/CS-PDA and PLGA/CS-PDA-bFGF groups, as illustrated in Fig. 4C. The illustration in Fig. 4D presents

the comparative assessment of reactive oxygen species (ROS) levels in RSC96 cells following H<sub>2</sub>O<sub>2</sub> induction, revealing notable distinctions between the PLGA/CS group and both the PLGA/CS-PDA group ( $P < 0.01$ ) and the PLGA/CS-PDA-bFGF group ( $P < 0.01$ ). Fig. 4E–G exhibit a substantial reduction in the proliferation of RSC96, PC12, and RAW264.7 cells subsequent to H<sub>2</sub>O<sub>2</sub> exposure, which is ascribed to the oxidative stress-induced damage caused by H<sub>2</sub>O<sub>2</sub>. In identical





**Fig. 6.** (A) Assessment of sciatic nerve function and electrical conduction recovery 12 weeks after surgery. (B) Typical 3D stress diagrams at twelve weeks after surgery. (C) Representative CMAP waveform of the injured side in each group. (D) Analysis of SFI values of all of the groups at twelve weeks after surgery. (E) statistical analysis of conduction velocity in each group. (F) statistical analysis of peak amplitude of CMAP in each group. (G) Representative images of gastrocnemius and Masson's staining of the cross sections from the injured side at twelve weeks after surgery. The left muscles were from the uninjured side, and those on the right were taken from the injured side. (H) Comparison of the wet weight ratios of gastrocnemius (injured muscle vs normal muscle) among autograft, PLGA/CS, PLGA/CS-PDA and PLGA/CS-PDA-bFGF groups. (I) Comparison of the mean cross-sectional area of muscle fibers from the injured side among autograft, PLGA/CS, PLGA/CS-PDA and PLGA/CS-PDA-bFGF groups. (n = 3,  $^{***}P < 0.01$ , versus PLGA/CS group;  $^{\#}P < 0.05$ , versus PLGA/CS-PDA group;  $^{##}P < 0.01$ , versus PLGA/CS-PDA group;  $^{\&}P < 0.05$ , versus PLGA/CS-PDA-bFGF group;  $^{\&}P < 0.01$ , versus PLGA/CS-PDA-bFGF group).



experimental conditions, pre-treatment with PLGA/CS-PDA and PLGA/CS-PDA-bFGF scaffolds resulted in a notable enhancement in cell viability compared to the H<sub>2</sub>O<sub>2</sub> group, as indicated by statistical significance ( $P < 0.01$ ). Conversely, the PLGA/CS scaffold did not elicit a substantial alteration in cell viability ( $P > 0.05$ ). The aforementioned findings highlight the efficacy of polydopamine (PDA) coating in scavenging reactive oxygen species (ROS) and confirming its antioxidant potential. PDA-coated surfaces contain abundant catechol groups that can engage in redox reactions with ROS, transforming them into more stable compounds like water and oxygen. Additionally, PDA can mitigate cellular harm by sequestering free radicals of reactive oxygen species (ROS). The exceptional biocompatibility and adhesion characteristics of polydopamine facilitate its strong attachment to cellular surfaces, thereby augmenting its ability to eliminate intracellular ROS [52]. The scavenging of reactive oxygen species by PDA can be attributed to the enrichment of its surface with catechol moieties, whose redox properties allow PDA to both quench reactive oxygen radicals by providing H atoms and to reduce reactive oxygen radicals via electron transfer [53]. In addition, there have also been studies/Shi's team studies that have found the presence of free radicals in PDA that can act as superoxide electrocatalytic centers [54]. The excellent biocompatibility and adhesion of PDA can enhance the tight binding between the scaffold and the cell surface, further enhancing the efficiency of scavenging reactive oxygen radicals.

Macrophages are vital components of the immune system and are integral in regulating the microenvironment following neural injury, thereby facilitating neural repair. Initially, macrophages display a pro-inflammatory (M1) phenotype to remove damaged neural tissue, before transitioning to an anti-inflammatory (M2) phenotype to support the repair of neural tissue [55]. In instances of peripheral nerve damage, there can be an overabundance of oxidative stress and inflammatory responses that obstruct the transformation of macrophages from the pro-inflammatory (M1) state to the anti-inflammatory (M2) state. This impediment can hinder the advancement of neural regeneration. In our research, our objective was to enhance the conditions for neural regeneration by counteracting elevated levels of reactive oxygen species (ROS) using polydopamine (PDA), consequently facilitating the shift of macrophages from the M1 to the M2 phenotype (refer to Fig. 4A). First, we used FITC/DAPI staining to observe the morphological changes of macrophages under the induced stimulation of LPS with IFN- $\gamma$ . Fig. 4H shows that macrophages in the control group exhibited a typical M1 phenotype rich in pseudopods, and the PLGA/CS group was similar to the control group. In the PLGA/CS-PDA and PLGA/CS-PDA-bFGF groups, there were significantly more macrophages with a shuttle-shaped M2 phenotype. We used an immunofluorescence staining assay to further investigate the changes in macrophage phenotype. As shown in Fig. 4H, we observed the expression of iNOS (M1-type macrophage marker) and Arg-1 (M2-type macrophage marker) in each group under interferon- and LPS-induced inflammatory conditions. Compared with the control group, the percentage of iNOS immunofluorescence was significantly decreased ( $p < 0.01$ ) and the percentage of Arg-1 immunofluorescence was significantly increased ( $p < 0.01$ ) in both PLGA/CS-PDA and PLGA/CS-PDA-bFGF groups (Fig. 4I–J). Morphological observations of macrophages and immunofluorescence staining results were consistent, further suggesting that PDA plays a role in regulating the conversion of macrophages from M1 to M2 phenotype. In addition, with the upregulation of inducible iNOS, these classically activated M1-type macrophages also produce a large number of pro-inflammatory factors. The expression of pro-inflammatory factors TNF- $\alpha$ , iNOS, and IL-6 was significantly downregulated in the PLGA/CS-PDA group and PLGA/CS-PDA-bFGF group, which was significantly lower than that in the PLGA/CS group (Fig. 4K–M). And the significant expression of Arg-1 was associated with the execution of tissue repair function of M2 macrophages, and the anti-inflammatory factor IL-10 in the PLGA/CS-PDA group and PLGA/CS-PDA-bFGF group was significantly higher than that in the PLGA/CS group ( $p <$

0.01) (Fig. 4N). In the pathological microenvironment of nerve injury, intracellular inflammation-related signaling pathways, such as neutrophils and monocytes, are activated under oxidative conditions, which subsequently promote the production of more inflammatory factors and reactive oxygen species. This vicious cycle ultimately leads to loss of calcium homeostasis, lipid peroxidation, mitochondrial dysfunction in neurons and thus hinders the repair of peripheral nerve injury. The antioxidant effect of PDA significantly ameliorates the vicious cycle in the pathological microenvironment of injury. From the results, the expression of pro-inflammatory factors (IL-6, TNF- $\alpha$ ) was significantly decreased in cells grown on scaffolds with PDA coating.

### 3.5. *In vivo* biocompatibility assessment

To further assess the biocompatibility of the scaffolds, they were implanted into the subcutaneous tissue of rat backs (refer to Fig. 5). Histological examination using HE staining revealed that the PLGA/CS group exhibited mild inflammation on the 3rd day, which had largely resolved by the 7th and 14th days. In contrast, the PLGA/CS-PDA group and the PLGA/CS-PDA-bFGF group showed no significant inflammatory response at any time point. Additionally, TNF- $\alpha$  and IL-6 immunofluorescence staining was utilized to evaluate the expression of inflammatory factors, with semi-quantitative analysis indicating a gradual decrease in the positive areas of both factors over time in all groups. Notably, the PLGA/CS-PDA and PLGA/CS-PDA-bFGF groups demonstrated superior performance compared to the PLGA/CS group ( $P < 0.01$ ), suggesting that the PDA coating effectively mitigates inflammation. These results support the conclusion that the scaffold can be considered a safe implant option.

### 3.6. Assessment of sciatic nerve function and electrophysiological recovery

A rat sciatic nerve defect model with a 10 mm gap was created for the purpose of studying the impact of the PLGA/CS-PDA-bFGF scaffold on nerve repair *in vivo*. Approval for all animal experiments was obtained from the Ethics Committee of Peking University People's Hospital under Ethics License No.: 2023PHE062.

Following a 12-week period post nerve injury, the evaluation of motor function recovery across various groups was conducted utilizing rat plantar pressure distribution, sciatic functional index, electrophysiological testing, muscle staining and wet weight, as well as muscle fiber area (refer to Fig. 6A). The rat plantar pressure distribution data is illustrated in Fig. 6B. Notably, in the PLGA/CS-PDA-bFGF group, the contact area and plantar pressure of the right hind limb exhibited significant improvement compared to the PLGA/CS and PLGA/CS-PDA groups, and were found to be comparable to those observed in the autograft group. The Sciatic Functional Index (SFI) is a commonly utilized quantitative approach for evaluating the motor function of the sciatic nerve in rats through the measurement of toe spread. The SFI scale spans from 0, indicating normal function, to -100, denoting complete impairment. The statistical findings depicted in Fig. 6D reveal that the SFI values within the PLGA/CS-PDA-bFGF group exhibited a notable increase compared to both the PLGA/CS group ( $p < 0.01$ ) and the PLGA/CS-PDA group ( $p < 0.01$ ), while being comparable to those observed in the autograft group. Electrophysiological assessments, as illustrated in Fig. 6C–E, and F, demonstrated that the conduction velocity in the PLGA/CS-PDA-bFGF group was slower than that in the autograft group ( $p < 0.01$ ), yet notably faster than in both the PLGA/CS group ( $p < 0.01$ ) and the PLGA/CS-PDA group ( $p < 0.05$ ). Furthermore, the compound muscle action potential amplitude in the PLGA/CS-PDA-bFGF group exhibited a significant increase in comparison to both the PLGA/CS group ( $p < 0.01$ ) and the PLGA/CS-PDA group ( $p < 0.01$ ), with no significant variance observed when compared to the autograft group.

Following sciatic nerve injury, muscles that lack nerve innervation experience notable atrophy, resulting in compromised motor function.

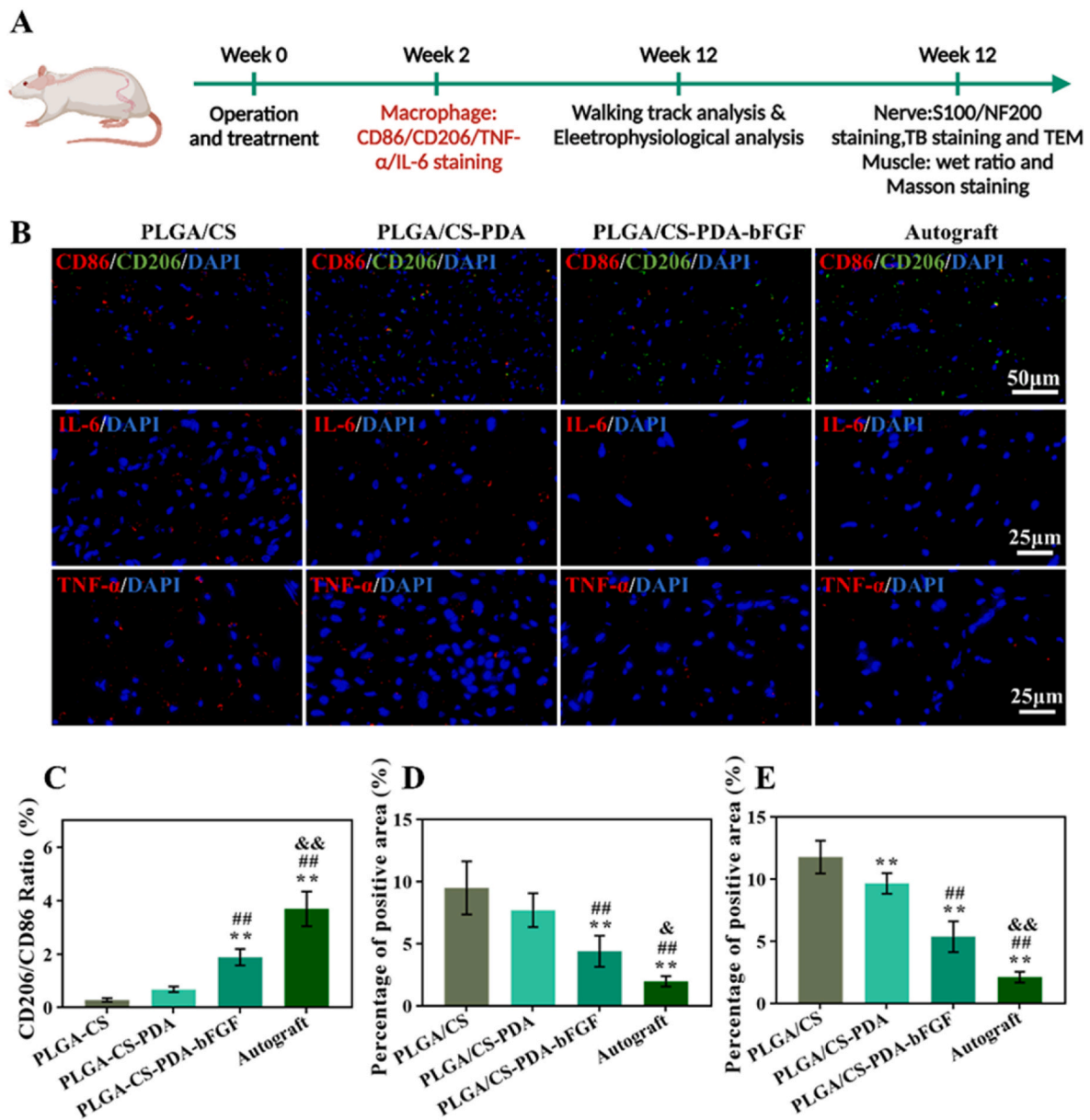


**Fig. 7.** (A) Evaluation of the regulatory effect of stents on in vivo immune response by CD86/CD206/IL-6/TNF- $\alpha$  staining at 2 weeks post surgery. (B) Analysis of immunofluorescence for CD86, CD206, IL-6 and TNF- $\alpha$  in tissue sections obtained from the regenerated nerves. (C) Comparison of the CD206/CD86 ratio among autograft, PLGA/CS, PLGA/CS-PDA and PLGA/CS-PDA-bFGF groups. (D,E) Statistical results of the percentage of IL-6 positive staining area and the percentage of TNF- $\alpha$  positive staining area (n = 6, \*\*P < 0.01, versus PLGA/CS group; ###P < 0.01, versus PLGA/CS-PDA group; &P < 0.05, versus PLGA/CS-PDA-bFGF group; &&P < 0.01, versus PLGA/CS-PDA-bFGF group).

The gross morphology image of the gastrocnemius muscle is depicted in Fig. 6H, illustrating varying levels of atrophy in the gastrocnemius muscle of the right hind limb across all experimental groups post-sciatic nerve injury. Masson's trichrome staining results are presented in Fig. 6G, revealing the presence of blue-stained collagen fibers in all groups. Muscle fiber morphology in the autograft and PLGA/CS-PDA-bFGF groups exhibited a more uniform appearance compared to the PLGA/CS and PLGA/CS-PDA groups. Analysis of muscle fiber cross-sectional area (Fig. 6I) indicated a significantly greater area in the PLGA/CS-PDA-bFGF group compared to the PLGA/CS group (p < 0.01) and the PLGA/CS-PDA group (p < 0.01), but lower than the autograft group (p < 0.05). These findings collectively suggest that the PLGA/CS-PDA-bFGF scaffold holds promise in mitigating denervated muscle atrophy, thereby potentially enhancing nerve regeneration.

### 3.7. Modulation of in vivo immune response by the scaffold

One of the primary obstacles in the restoration of peripheral nerve function lies in the regulation of the immune microenvironment. The inflammatory response that ensues following peripheral nerve damage has the potential to disrupt the surrounding environment, thereby impeding the subsequent process of nerve regeneration. Macrophages play a crucial role in signaling early inflammation. In the context of peripheral nerve injury recovery, macrophages typically undergo a transition from a pro-inflammatory phenotype (M1) aimed at clearing damaged nerve tissue to an anti-inflammatory phenotype (M2) that facilitates nerve tissue repair [55]. In order to evaluate the inflammatory modulation of early peripheral nerve injury subsequent to the introduction of scaffolds within each experimental cohort, we conducted immunostaining for CD86/CD206, TNF- $\alpha$ , and IL-6 to assess M1 and M2

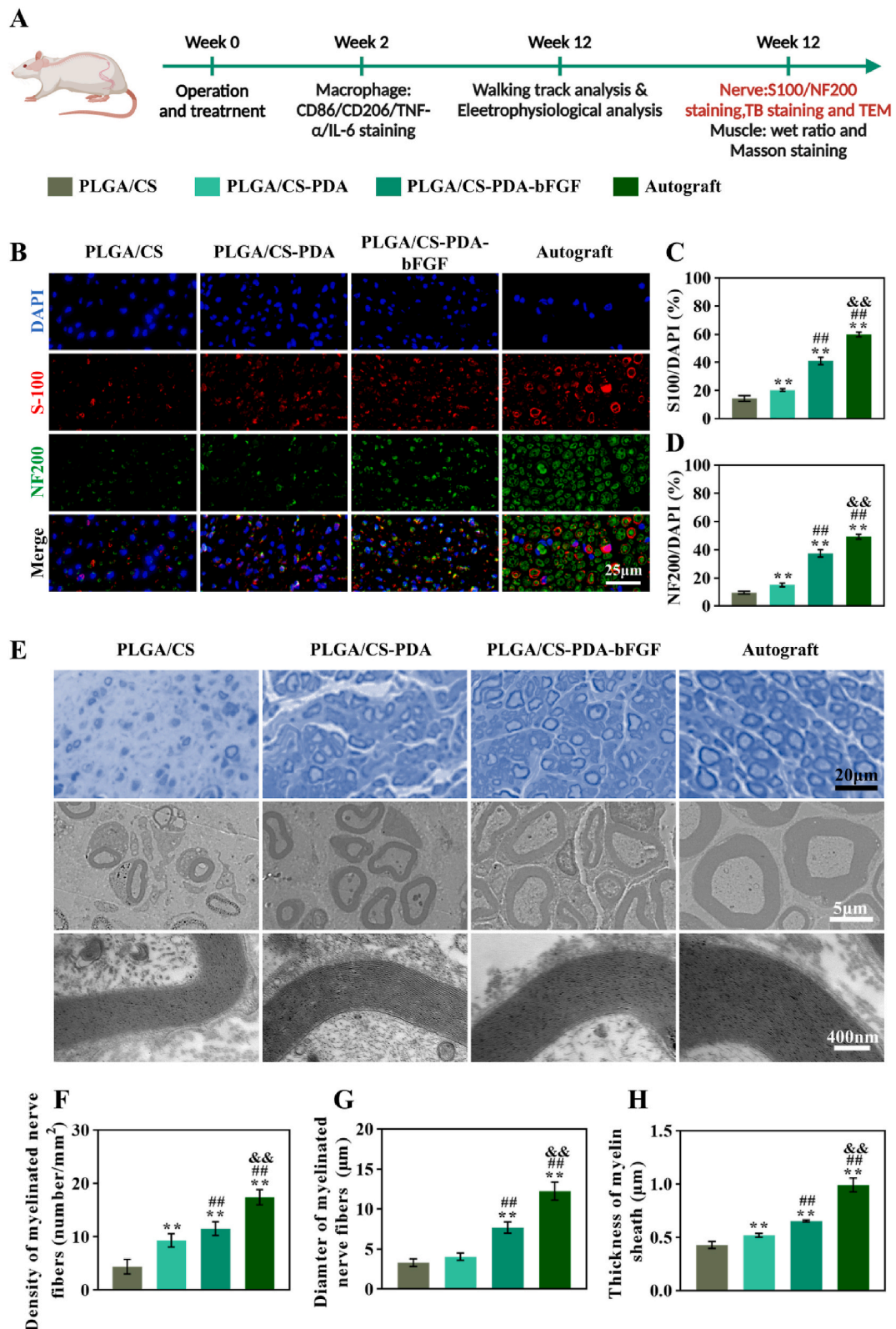


**Fig. 8.** (A) Analysis of histological and ultrastructural characteristics of regenerated nerves at 12 weeks post surgery. (B) Double-immunofluorescent staining of the Schwann cell marker S100 (red) and the axon marker NF200 (green) of cross-sections of the middle segments of regenerated nerves. (C,D) Statistical results of the percentage of S100 positive staining area and the percentage of NF200 positive staining area (n = 6). (E) Toluidine blue staining, TEM images and Enlarged TEM image of cross-sections of the distal segments of regenerated nerves. (F-G) Statistical results of the density of the myelinated nerve fibers, the diameter of the myelinated nerve fibers and the thickness of the myelin sheath (n = 10). \*\*P < 0.01, versus PLGA/CS group; ###P < 0.01, versus PLGA/CS-PDA group; &&P < 0.01, versus PLGA/CS-PDA-bFGF group.



macrophages and their production of inflammatory mediators in nerve tissues at the 2-week postoperative mark (refer to Fig. 7A). The outcomes are depicted in Fig. 7B–E. The ratio of M2/M1 positive areas was elevated in the PLGA/CS-PDA and PLGA/CS-PDA-bFGF groups in comparison to the PLGA/CS group, yet lower than that observed in the autograft group ( $p < 0.01$ ). The expression levels of IL-6 and TNF- $\alpha$  were notably reduced in the PLGA/CS-PDA and PLGA/CS-PDA-bFGF groups relative to the PLGA/CS group ( $p < 0.01$ ), although they were higher compared to the autograft group ( $p < 0.05$ ). The findings suggest that PLGA/CS-PDA and PLGA/CS-PDA-bFGF demonstrate significant anti-inflammatory properties in the initial phases of peripheral nerve damage. This efficacy is linked to the inclusion of polydopamine (PDA), which plays a role in modulating the conversion of M1 macrophages to M2 macrophages. These results align with outcomes observed in laboratory-based investigations [56].

### 3.8. Histological evaluation of regenerated nerves

Following a 12-week period post-surgery, an examination of the histological and ultrastructural features of regenerated nerves was conducted. Fig. 8A illustrates the results of this analysis. Fig. 8B–D displays the outcomes of immunofluorescence staining for S100/NF200. The immunohistochemical analysis revealed that the expression levels of S100 and NF200 in the PLGA/CS-PDA-bFGF group were significantly greater compared to those in the PLGA/CS group ( $P < 0.01$ ) and the PLGA/CS-PDA group ( $P < 0.01$ ). Notably, the autograft group exhibited the highest positive area. Furthermore, the PLGA/CS-PDA group demonstrated a higher positive area of S100 and NF200 in comparison to the PLGA/CS group ( $P < 0.01$ ). The staining of toluidine blue in the mid-section interface and the examination of myelin sheath through transmission electron microscopy are depicted in Fig. 8E. The autograft group exhibited the highest nerve density, followed by the PLGA/CS-PDA-bFGF group and the PLGA/CS-PDA group (Fig. 8F). The myelinated nerve fiber diameter and myelin sheath thickness were notably greater in the PLGA/CS-PDA-bFGF group compared to the PLGA/CS group and the PLGA/CS-PDA group ( $p < 0.01$ ), yet lower than those observed in the autograft group ( $p < 0.01$ ) (Fig. 8G–H). These findings suggest that the utilization of the PLGA/CS-PDA-bFGF scaffold holds promise for replacing autografts in the treatment of nerve injuries.

### 3.9. The mechanism of action of PLGA/CS-PDA-bFGF in peripheral nerve regeneration

The recovery process following peripheral nerve injury is intricate, involving various cellular events such as macrophage migration to the injury site for debris clearance, Schwann cell proliferation and migration to form Büngner bands, and axonal elongation to restore connections with distant organs. The scaffold developed in this research, composed of PLGA/CS-PDA-bFGF, exhibits superior mechanical properties that offer a stable environment for long-term nerve regeneration. Through its ability to promptly clear reactive oxygen species and modulate macrophage polarization from M1 to M2, the scaffold safeguards nascent cells from oxidative stress-induced damage and facilitates unimpeded progression of neural regenerative processes. The adjustment of the PDA coating enhances the scaffold's hydrophilicity and introduces active functional groups, facilitating cell adhesion and migration. Additionally, the scaffold's aligned topographical structure promotes directional growth of Schwann cells and nerve cells along the fibers. The sustained release of bFGF, achieved through robust covalent bonding, sustains neural tissue regeneration over an extended period. These combined factors are strategically aligned to address distinct functional needs during various stages of injury repair, thereby synergistically enhancing the functional regeneration of peripheral nerves.

## 4. Conclusion

In brief, a nerve conduit comprising oriented nanofibers of PLGA/CS, developed through electrospinning and PDA coating techniques, is proposed in this study. This conduit combines natural and synthetic materials along with biologically active molecules. The aligned fiber structure offers a stable environment for nerve regeneration and guides the growth of nerve cells in a specific direction. The PDA coating serves to shield newly formed cells from oxidative stress during the initial stages and actively influences the immune microenvironment to create conducive conditions for nerve regeneration. Additionally, the incorporation of the biologically active molecule bFGF enables sustained and controlled release over an extended period by gradual degradation of the coating and cleavage of covalent bonds. The PLGA/CS-PDA-bFGF nerve conduit is designed to effectively address the diverse requirements of nerve regeneration stages, facilitating the restoration of damaged nerve structure and function. In conclusion, the multifunctional PDA-coated nerve conduit, in conjunction with biologically active molecules, is anticipated to offer novel perspectives for mending peripheral nerve injuries.

### CRediT authorship contribution statement

**Xiaokun Chen:** Writing – original draft, Methodology, Investigation, Formal analysis, Data curation, Conceptualization. **Jihai Xu:** Writing – original draft, Methodology, Investigation, Formal analysis, Data curation, Conceptualization. **Feng Qin:** Writing – review & editing, Methodology, Investigation, Formal analysis, Data curation, Conceptualization. **Ziyuan Yang:** Methodology, Investigation, Formal analysis, Data curation. **Xueyuan Li:** Supervision, Software, Formal analysis, Data curation. **Miao Yu:** Visualization, Validation, Supervision. **Ming Li:** Writing – review & editing, Supervision, Software, Resources, Methodology, Funding acquisition, Conceptualization. **Yanhua Wang:** Visualization, Resources, Project administration, Methodology, Funding acquisition, Conceptualization. **Wang Xin:** Validation, Supervision, Methodology, Funding acquisition, Conceptualization.

### Declaration of competing interest

The authors declare that they have no known competing financial interests or personal relationships that could have appeared to influence the work reported in this paper.

### Acknowledgments

This work was financially supported by National Key R&D Program of China(2022YFC3006200), Natural Science Foundation of China (81901251,31640045), Beijing Natural Science Foundation (L244068,7204323,7232190), Ningbo Top Medical and Health Research Program (No.2022020506), Ningbo Science and Technology Planning Project (2022S058) and Zhejiang Province Medical and Health Technology Planning Project(2024KY1615).

### Appendix A. Supplementary data

Supplementary data to this article can be found online at <https://doi.org/10.1016/j.mtbio.2025.101543>.

### Data availability

Data will be made available on request.

### References

- [1] P.N. Mohanna, et al., A composite poly-hydroxybutyrate-glia growth factor conduit for long nerve gap repairs, *J. Anat.* 203 (6) (2003) 553–565.



- [2] B. Lopes, et al., Peripheral nerve injury treatments and advances: one Health perspective, *Int. J. Mol. Sci.* 23 (2) (2022).
- [3] R. Li, et al., Peripheral nerve injuries treatment: a systematic review, *Cell Biochem. Biophys.* 68 (3) (2014) 449–454.
- [4] S. Kehoe, X.F. Zhang, D. Boyd, FDA approved guidance conduits and wraps for peripheral nerve injury: a review of materials and efficacy, *Injury* 43 (5) (2012) 553–572.
- [5] S. Yi, L. Xu, X. Gu, Scaffolds for peripheral nerve repair and reconstruction, *Exp. Neurol.* 319 (2019) 112761.
- [6] G. Keilhoff, et al., Peripheral nerve tissue engineering: autologous Schwann cells vs. transdifferentiated mesenchymal stem cells, *Tissue Eng.* 12 (6) (2006) 1451–1465.
- [7] T. Kornfeld, P.M. Vogt, C. Radtke, Nerve grafting for peripheral nerve injuries with extended defect sizes, *Wien. Med. Wochenschr.* 169 (9–10) (2019) 240–251.
- [8] X. Gu, et al., Construction of tissue engineered nerve grafts and their application in peripheral nerve regeneration, *Prog Neurobiol* 93 (2) (2011) 204–230.
- [9] X. Gu, F. Ding, D.F. Williams, Neural tissue engineering options for peripheral nerve regeneration, *Biomaterials* 35 (24) (2014) 6143–6156.
- [10] J. Du, et al., Biomimetic neural scaffolds: a crucial step towards optimal peripheral nerve regeneration, *Biomater. Sci.* 6 (6) (2018) 1299–1311.
- [11] G. Yang, et al., From nano to micro to macro: electrospun hierarchically structured polymeric fibers for biomedical applications, *Prog. Polym. Sci.* 81 (2018) 80–113.
- [12] J. Cheng, et al., Electrospinning versus microfluidic spinning of functional fibers for biomedical applications, *Biomaterials* 114 (2017) 121–143.
- [13] A.J. Reid, et al., N-Acetylcysteine alters apoptotic gene expression in axotomized primary sensory afferent subpopulations, *Neurosci. Res.* 65 (2) (2009) 148–155.
- [14] A. Faroni, et al., Peripheral nerve regeneration: experimental strategies and future perspectives, *Adv. Drug Deliv. Rev.* 82–83 (2015) 160–167.
- [15] R. Deumens, et al., Repairing injured peripheral nerves: bridging the gap, *Prog Neurobiol* 92 (3) (2010) 245–276.
- [16] I. Allodi, E. Udina, X. Navarro, Specificity of peripheral nerve regeneration: interactions at the axon level, *Prog Neurobiol* 98 (1) (2012) 16–37.
- [17] X. Dong, et al., An injectable and adaptable hydrogen sulfide delivery system for modulating neuroregenerative microenvironment, *Sci. Adv.* 9 (51) (2023) eadi1078.
- [18] S. Zhu, et al., A synthetic oxygen carrier-olfactory ensheathing cell composition system for the promotion of sciatic nerve regeneration, *Biomaterials* 35 (5) (2014) 1450–1461.
- [19] D. Li, Y.L. Wang, Y.N. Xia, Electrospinning of polymeric and ceramic nanofibers as uniaxially aligned arrays, *Nano Lett.* 3 (8) (2003) 1167–1171.
- [20] D. Li, Y.L. Wang, Y.N. Xia, Electrospinning nanofibers as uniaxially aligned arrays and layer-by-layer stacked films, *Adv. Mater.* 16 (4) (2004) 361–366.
- [21] Y. Wang, et al., Biocompatibility evaluation of electrospun aligned poly (propylene carbonate) nanofibrous scaffolds with peripheral nerve tissues and cells in vitro, *Chin Med J (Engl)* 124 (15) (2011) 2361–2366.
- [22] J. Wang, et al., The cellular response of nerve cells on poly-L-lysine coated PLGA-MWCNTs aligned nanofibers under electrical stimulation, *Mater Sci Eng C Mater Biol Appl* 91 (2018) 715–726.
- [23] H. Cheong, et al., Multi-dimensional bioinspired tactics using an engineered mussel protein glue-based nanofiber conduit for accelerated functional nerve regeneration, *Acta Biomater.* 90 (2019) 87–99.
- [24] M.N. Kumar, et al., Chitosan chemistry and pharmaceutical perspectives, *Chem Rev* 104 (12) (2004) 6017–6084.
- [25] E. Khor, L.Y. Lim, Implantable applications of chitin and chitosan, *Biomaterials* 24 (13) (2003) 2339–2349.
- [26] M. Sittinger, et al., Resorbable polyesters in cartilage engineering: affinity and biocompatibility of polymer fiber structures to chondrocytes, *J. Biomed. Mater. Res.* 33 (2) (1996) 57–63.
- [27] J. Acheta, et al., Therapeutic low-intensity ultrasound for peripheral nerve regeneration - a Schwann cell perspective, *Front. Cell. Neurosci.* 15 (2022).
- [28] B. Shen, F. Pei, Research progress in role of controlled release microsphere of basic fibroblast growth factor in promoting peripheral nerve regeneration, *Chin. J. Traumatol.* 21 (3) (2005) 233–236.
- [29] X. Xing, et al., PROTECTIVE EFFECTS OF bFGF DURING CEREBRAL ISCHEMIA AND REPERFUSION IN HIPPOCAMPUS AND CORTEX OF RATS, *Chinese Journal of Histochemistry and Cytochemistry* 17 (2) (2008) 160–163.
- [30] P.F. Tang, et al., Mussel-inspired electroactive and antioxidative scaffolds with incorporation of polydopamine-reduced graphene oxide for enhancing skin wound healing, *Acs Applied Materials & Interfaces* 11 (8) (2019) 7703–7714.
- [31] Y.L. Liu, K.L. Ai, L.H. Lu, Polydopamine and its derivative materials: synthesis and promising applications in energy, environmental, and biomedical fields, *Chem. Rev.* 114 (9) (2014) 5057–5115.
- [32] M. Bao, et al., ROS Scavenging and inflammation-directed polydopamine nanoparticles regulate gut immunity and flora therapy in inflammatory bowel disease, *Acta Biomater.* 161 (2023) 250–264.
- [33] T. Zhu, et al., Biofunctionalized composite scaffold to potentiate osteoconduction, angiogenesis, and favorable metabolic microenvironment for osteonecrosis therapy, *Bioact. Mater.* 9 (2022) 446–460.
- [34] Y. Qian, et al., Functional nanomaterials in peripheral nerve regeneration: scaffold design, chemical principles and microenvironmental remodeling, *Mater. Today* 51 (2021) 165–187.
- [35] Y. Qian, et al., An integrated multi-layer 3D-fabrication of PDA/RGD coated graphene loaded PCL nanoscaffold for peripheral nerve restoration, *Nat. Commun.* 9 (2018).
- [36] X.Y. Yao, et al., Metal organic framework-modified bioadaptable implant potentiates the reconstruction of nerve microenvironment via immunometabolism reprogramming, *Nano Today* 49 (2023).
- [37] X.Y. Yao, et al., Non-electric bioelectrical analog strategy by a biophysical-driven nano-micro spatial anisotropic scaffold for regulating stem cell niche and tissue regeneration in a neuronal therapy, *Bioact. Mater.* 20 (2023) 319–338.
- [38] J.T. Kan, et al., A novel botanical formula prevents diabetes by improving insulin resistance, *BMC Compl. Alternative Med.* 17 (2017).
- [39] H. Hu, et al., Polydopamine-Pd nanozymes as potent ROS scavengers in combination with near-infrared irradiation for osteoarthritis treatment, *iScience* 26 (5) (2023).
- [40] N. Fauchoux, et al., Self-assembled monolayers with different terminating groups as model substrates for cell adhesion studies, *Biomaterials* 25 (14) (2004) 2721–2730.
- [41] Y. Shen, et al., Advances of research of hydrophilic/hydrophobic surface effect on cell biologic behaviors in vitro, *Sheng wu yi xue gong cheng xue za zhi = Journal of biomedical engineering = Shengwu yixue gongchengxue zazhi* 28 (6) (2011) 1237–1241.
- [42] K. Abe, H. Saito, Effects of basic fibroblast growth factor on central nervous system functions, *Pharmacol. Res.* 43 (4) (2001) 307–312.
- [43] M. Li, et al., Nerve growth factor-basic fibroblast growth factor poly-lactide co-glycolid sustained-release microspheres and the small gap sleeve bridging technique to repair peripheral nerve injury, *Neural Regeneration Research* 18 (1) (2023) 162–169.
- [44] H.B. Si, et al., Control-released basic fibroblast growth factor-loaded poly-lactic-co-glycolic acid microspheres promote sciatic nerve regeneration in rats, *Exp. Ther. Med.* 13 (2) (2017) 429–436.
- [45] H. Lee, J. Rho, P.B. Messersmith, Facile conjugation of biomolecules onto surfaces via mussel adhesive protein inspired coatings, *Adv Mater* 21 (4) (2009) 431–434.
- [46] C.K. Poh, et al., The effect of VEGF functionalization of titanium on endothelial cells in vitro, *Biomaterials* 31 (7) (2010) 1578–1585.
- [47] C. Wei, et al., Advances of Schwann cells in peripheral nerve regeneration: from mechanism to cell therapy, *Biomed. Pharmacother.* 175 (2024) 116645.
- [48] Y. Cui, et al., Collagen scaffolds modified with CNTF and bFGF promote facial nerve regeneration in minipigs, *Biomaterials* 35 (27) (2014) 7819–7827.
- [49] S. Xue, et al., Phase separation on cell surface facilitates bFGF signal transduction with heparan sulphate, *Nat. Commun.* 13 (1) (2022).
- [50] Y. Tai, et al., Enhanced peripheral nerve regeneration by mechano-electrical stimulation, *NPJ Regen. Med.* 8 (1) (2023) 57.
- [51] M. Friedrich, M. Pohin, F. Powrie, Cytokine networks in the pathophysiology of inflammatory bowel disease, *Immunity* 50 (4) (2019) 992–1006.
- [52] Y.Z. Li, et al., Polydopamine-mediated graphene oxide and nanohydroxyapatite-incorporated conductive scaffold with an immunomodulatory ability accelerates periodontal bone regeneration in diabetes, *Bioact. Mater.* 18 (2022) 213–227.
- [53] J.H. Zhang, et al., ROS scavenging biopolymers for anti-inflammatory diseases: classification and formulation, *Adv. Mater. Interfac.* 7 (16) (2020).
- [54] Y.L. Liu, et al., Comprehensive insights into the multi-antioxidative mechanisms of melanin nanoparticles and their application to protect brain from injury in ischemic stroke, *J. Am. Chem. Soc.* 139 (2) (2017) 856–862.
- [55] Y. Xiang, et al., Research progress in immune microenvironment regulation of muscle atrophy induced by peripheral nerve injury, *Life Sci.* 287 (2021) 120117.
- [56] X.F. Bao, et al., Polydopamine nanoparticles as efficient scavengers for reactive oxygen species in periodontal disease, *ACS Nano* 12 (9) (2018) 8882–8892.